Tribology at the atomic scale with density functional theory

Hande Ustunel[1,*] **and Daniele Toffoli**[2,*]

[1] Department of Physics, Middle East Technical University, Dumlupinar Blv 1, 06800, Ankara, Turkey
[2] Dipartimento di Scienze Chimiche e Farmaceutiche, Università degli Studi di Trieste, Via L. Giorgieri 1, I-34127, Trieste, Italy
[*] Authors to whom any correspondence should be addressed.

E-mail: ustunel@metu.edu.tr and toffoli@units.it

Keywords: tribology, density functional theory, friction, passivation, lubricants, dissipation

Abstract

Understanding the quantum mechanical origins of friction forces has become increasingly important in the past decades with the advent of nanotechnology. At the nanometer scale, the universal Amontons–Coulomb laws cease to be valid and each interface requires individual scrutiny. Furthermore, measurements required to understand friction at the atomic scale are riddled with artificial factors such as the properties of the friction force microscope, effect of the environment, and the type of the substrate. It therefore proves difficult to isolate the actual behavior of interfaces from these effects. Electronic structure methods are an indispensable tool in understanding the details of interfaces, their interactions with lubricants, the environment and the support. In particular, density functional theory (DFT) has given large contributions to the field through accurate calculations of important properties such as the potential energy surfaces, shear strengths, adsorption of lubricant materials and the effect of the substrate. Although unable to tackle velocity- or temperature-dependent properties for which classical molecular dynamics is employed, DFT provides an affordable yet accurate means of understanding the quantum mechanical origins of the tribological behavior of interfaces in a parameter-free manner. This review attempts to give an overview of the ever-increasing literature on the use of DFT in the field of tribology. We start by summarizing the rich history of theoretical work on dry friction. We then identify the figures-of-merit which can be calculated using DFT. We follow by a summary of bulk interfaces and how to reduce friction via passivation and lubricants. The following section, namely friction involving two-dimensional materials is the focus of our review since these materials have gained increasing traction in the field thanks to the advanced manufacturing and manipulation techniques developed. Our review concludes with a brief touch on other interesting examples from DFT tribology literature such as rolling friction and the effect of photoexcitation in tribology.

1. Introduction

Our phenomenological understanding of friction at the interface of macroscopic bodies in relative motion has been shaped throughout the past several centuries. While Amontons' laws work at these scales, their fundamental assumptions begin to fail at the atomic level. At this scale, friction coefficients turn out to be both load- [1] and velocity-dependent [2] while quantum mechanical effects can no longer be ignored. With the advent of fabrication and characterization of materials at the nanoscale, tribological behavior of materials has become experimentally accessible thanks to atomic force microscopy (AFM) [3] and friction force microscopy (FFM) [4]. A solid theoretical understanding to accompany, explain and predict the outcome of these experiments via numerical models and simulations has become imperative.

The first models of the atomistic mechanisms of dry friction were established as early as the late 1920s. The two works that initiated the field are universally accepted to be the 1928 paper by Prandtl [5] and the 1929 paper by Tomlinson [6]. In spite of some ambiguity with the naming convention uncovered by Popov [7], the earliest atomistic description came to be called the Prandtl–Tomlinson (PT) model. The PT model is a simplified representation of an AFM sliding experiment where the AFM cantilever and tip are replaced by two

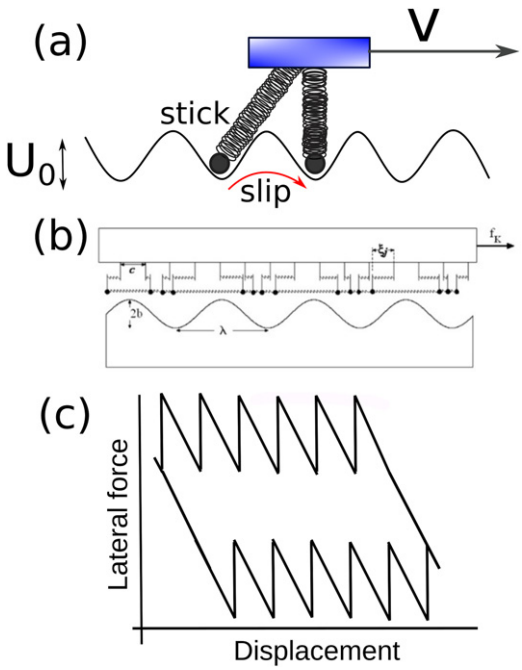

Figure 1. (a) The PT model. A sliding object moves with a constant speed along a straight line dragging a second object of mass m along a surface. The surface is modeled by a sinusoidal potential of amplitude U_0. (b) A sketch of the FKT model. A generalization of the PT model where the sliding object is replaced by a periodic array of masses. (c) Illustration of a typical stick–slip loop resulting from forward–backward scan in the PT model. The energy dissipated can be found by integrating the area between the two curves. (b) and (c) Reprinted from [20], Copyright (2011), with permission from Elsevier

point masses attached via a spring and the underlying substrate by a sinusoidal potential (see figure 1(a)). A periodic extension of the PT model was developed in combination with the more general Frenkel–Kontorova ball-and-chain model, which was originally formulated for atomic dynamics near dislocations in crystals [8]. Usually referred to as the Frenkel–Kontorova–Tomlinson model (FKT) (see figure 1(b)), it improves the point particle description of the AFM tip by replacing it with a chain of atoms sliding over the periodic potential. This allows for the inclusion of the elasticity of the sliding layer or object. In the years since these models were introduced, many variations, additions and improvements were developed. For instance, in a series of publications starting in 1992, Sokoloff [9–11] introduced complex models taking into account the crystallinity of the substrate in two and three dimensions as well [12]. In time, these models evolved further in complexity and were mostly replaced by modern classical molecular dynamics (MD) simulations [13–18]. However, nearly a century later, PT and FKT models are still actively investigated [19].

A quantum mechanical description of friction was first introduced by Zhong and Tománek [21], who illustrated the calculation of the lateral friction forces and eventually the friction coefficient for a model system of a single Pd atom sliding on a Pd surface using density functional theory (DFT) [22]. In their work, Zhong and Tománek outlined a simple method for calculating the load-dependent friction forces and average friction coefficients. This recipe then started an avalanche in the field of computational tribology, resulting in a very large number of publications every year [12, 23, 24].

Research in modern tribology at the nanoscale is mostly conducted using one of two families of methods. Classical MD work, which relies on accurate interatomic potentials can model larger systems, longer times, finite temperatures, and some experimental features such as the shape of the AFM tip. On the other hand, electronic structure methods, most commonly DFT, are restricted to smaller simulation cells, and often to zero temperature. *Ab initio molecular dynamics (AIMD)* has become increasingly more available with improving computational resources and innovative algorithms [25]. However, it still remains restricted to short time scales on the order of hundreds of picoseconds, while the time scales of interest are usually at least several nanoseconds. While restricted in size and length, static DFT methods have the potential to accurately describe key figures of merit such as interfacial interactions and charge transfer [26].

A comprehensive review, doing justice to the vast field of atomic-scale tribology is impossible. In this review, we therefore focus specifically on the contributions of the DFT community to this field. The approach taken in this review is to first introduce the key materials properties that can be reliably calculated within DFT and then present a large number of examples from diverse systems studied using this method. As such, our review is organized based on the properties calculated rather than focusing on a particular class of systems. The review is structured as follows. We first start with a brief identification of key features of the friction problem that

can be reliably calculated using DFT methods. We then present a review on perfect bulk and two-dimensional interfaces. Next, we review works on systems with imperfections such as defects, and impurities. Finally, we present an overview of an emerging subfield of friction, namely nanotribology. For reviews of other aspects of the field, we refer to reader to the many excellent works that have come out in the last ten years [12, 27–30].

2. Origins and figures of merit of friction

Historically, atomic origins of friction were uncovered first via numerous simple models [5, 6]. Although mostly replaced by large-scale classical MD simulations, these early works still hold an important place in modern tribology literature for highlighting the important properties of the materials in contact, the interface, and the sliding experiment. The PT model (figure 1(a)) represents the interface between a perfect crystal surface and a sliding object, such as an AFM tip, by a periodic potential with a height U_0 and periodicity a. The equation of motion describing the motion of the sliding object is [7]:

$$m\ddot{x}(t) = k(v_0 t - x(t)) - \eta\dot{x}(t) - U_0 \sin(2\pi x(t)/a), \tag{1}$$

where k is the spring constant between the driving and the sliding particles, and v_0 is the constant speed of the driving object. A phenomenological damping coefficient η is added to represent the velocity-dependent loss term. Finally, $x(t)$ is the current position of the sliding object. The lateral force on the sliding object is the friction force, used to define the friction coefficient using

$$\mu = \frac{F_\mathrm{f}}{F_\mathrm{L}} \tag{2}$$

where F_L is the vertical load. Equation (1) reveals interesting and complex physics. The elasticity of the sliding object is modeled by a harmonic spring with spring constant k. Depending on the relation between U_0 and k, sliding can occur in a continuous manner or with sudden jumps of the sliding object between the minima on the potential energy surface (PES). If the spring is soft enough, the juxtaposition of the sinusoidal profile and the quadratic potential energy from the spring results in a series of local minima. As the object slides, it gets stuck in these minima until the spring is stretched far enough to overcome the barrier and cause the sliding object to suddenly jump from one minimum to the next (figure 1(a)). Each jump is followed by an energy build-up phase where the object is stationary as the spring stretches until the next jump occurs. This discontinuous motion is termed the *stick–slip* regime. A part of the energy stored during the stick phase is released during the slip phase and is lost to the vibrational degrees of freedom of one or both of the systems in contact. On the other hand, if the spring is sufficiently stiff, the sliding object will follow the driver continuously. Through some simplifying assumptions (such as small velocity), the critical stiffness that defines the boundary between the two regimes of motion can be calculated as (following Popov's treatment [7])

$$k_\mathrm{c} = U_0 \frac{2\pi}{a}. \tag{3}$$

The stick–slip regime is characterized by the well-known sawtooth profile of the friction force and a hysteresis effect in a back-and-forth scan (figure 1(c)). The area between the back and forth scan lines represents the amount of energy that is available to be dissipated. In the continuous regime, no energy is lost to friction via atomic vibrations. This regime is usually referred to as the *superlubric regime*. Since the physics of an actual problem is more complicated than this model, it is difficult to predict the point where (or if) such an instability may occur. Hence, the term superlubric has come to be used for very low friction (usually a friction coefficient satisfying $\mu < 0.01$ [31]) in a given interface. In a real system, k is replaced by the shear strength of the material and the sinusoidal profile by an actual map of the total interaction energy. Both of these properties can be calculated within the DFT framework.

The PT model, under the assumption of a soft spring [7], also yields the dependence of the friction force on the velocity as

$$F = F_\mathrm{C} - \left|\alpha k_\mathrm{B} T \ln\left(\frac{v_\mathrm{c}}{v}\right)^{2/3}\right| \tag{4}$$

where F_C is the maximum value of the friction force at zero temperature, α is a parameter dependent on the shape of the potential, k_B is the Boltzmann constant, v is the velocity of the sliding object, v_c is the critical velocity beyond which the friction force becomes velocity independent. While the second term cannot be handled with a static calculation, the first term depends only on barrier height against sliding and can therefore be calculated accurately with DFT.

The FKT model extends the sliding object to a bulk surface and takes into account its internal structure (figure 1(b)). The height of the potential energy is b and its wavelength is λ. The equilibrium distance between

masses in the sliding object is c and the displacement of the ith object with respect to its equilibrium position is ξ_i. Built upon the Frenkel–Kontorova model, which was first formulated as a general purpose simple representation of two interacting periodic structures in one dimension, the FKT model can be seamlessly applied to the friction problem.

Over the past decades, the simplicity of these models has made possible the investigation of the effect of a very large set of parameters on the nanotribological properties of the interface. Among these are velocity of the sliding object [32], vertical load [33] and temperature [34]. Unfortunately any of these properties that require a long-time simulation or a large number of atoms is not viable for the typical DFT calculation. Although MD is not limited to classical interatomic potentials, it is much more challenging to perform an MD simulation using *ab initio* methods. The time scales needed for an accurate simulation are far larger than those that can be realistically achieved [35]. Therefore parameters such as velocity and temperature are difficult, if not impossible, to investigate via electronic structure methods. On the other hand, the following relevant properties can be reliably calculated using modern electronic structure methods:

(a) *PES, the minimum-energy path (MEP) and corrugation* The PES of an interface refers to the total energy of the two materials as a function of their relative positions. To map the PES, the two materials making up the interface are displaced systematically along a two dimensional grid within the boundaries of their joint simulation cell. Assuming that the interface lies on the xy plane, the PES is mapped by calculating the energy at the minimum energy separation of the two materials at each point (x, y) on a smaller number of points on the grid. The rough PES thus obtained is usually interpolated between the grid points. Since only energy differences are relevant, the PES is often calculated in reference to its global minimum using

$$E(x, y, z_0) = E_{\text{tot}}(x, y, z_0) - E_{\text{min}} \tag{5}$$

where x and y correspond to the relative displacement of the two surfaces with respect to some reference location. z_0 indicates the height that yields the minimum energy for a given x and y:

$$E_{\text{tot}}(x, y, z_0) = \min_z E_{\text{tot}}(x, y, z). \tag{6}$$

The right panel of figure 2 displays a typical example of a PES between two Cu(111) surfaces. As shown in this figure, the PES is characterized by energy minima, maxima and saddle points. The path highlighted with a dashed line is the so-called MEP, which is the preferred path of travel as one of the interfaces slide against the other.

The most decisive property to be derived from the PES regarding the friction forces is the difference between the maximum and the minimum of the PES, referred to as the *corrugation*,

$$\Delta E = E_{\text{max}} - E_{\text{min}}. \tag{7}$$

The corrugation corresponds to the potential height in the PT model. An estimate for an upper limit of the friction forces can be obtained by dividing the corrugation by the distance between the minimum and the maximum along the path of travel,

$$F_{\text{f}} \approx \frac{\Delta E}{\Delta \ell}. \tag{8}$$

Since all of the quantities listed here are dependent on ground-state energy differences, DFT is expected to perform well and correctly represent reality. The first fully DFT-based investigation of the tribological properties of an interface is commonly accepted to be the work by Zhong and Tománek [21]. In their work a Pd atom is pulled along a straight line on hexagonal graphite. The mean friction force was approximated by dividing the maximum of the PES by the distance traveled in one spatial period. The load dependence was explored by adjusting the vertical distance (z) of the Pd atom at each horizontal location (x) to yield the desired load. Since the publication of this seminal paper, most DFT works devoted to the study of bulk interfaces used similar methods. More recently, Cahangirov *et al* presented a straightforward way of translating the DFT PES data to stick–slip criteria [36], establishing the link between phenomenological parameters such as the stick–slip threshold and atomistic DFT results. The conclusion from this body of work is that a lower corrugation correlates with lower friction forces and can be evidence for motion in the continuous sliding regime.

(b) *Energy of adhesion:* related to the PES is the energy of adhesion (E_{adh}), which is the work needed to put together the two surfaces to form the interface. E_{adh} is calculated using:

$$E_{\text{adh}} = E_{\text{int}} - E_{s1} - E_{s2} \tag{9}$$

where E_{int} is the total energy of the two surfaces of the interface at the global minimum and the equilibrium separation, while E_{s1} and E_{s2} refer to the energies of the two surfaces in isolation. Since the energy of

adhesion is an extensive quantity, it is usually reported per area or per atom. The energy of adhesion does not directly determine the magnitude of the friction force, however, it is important for determining the contact area in AFM experiments.

The negative of the adhesion energy, called the *energy of separation*, is also used often in describing the strength of interaction between the two sliding surfaces. The energy of separation can be interpreted as the work needed to separate the two surface to infinite distance.

(c) *Shear strength:* the shear strength of an interface τ_S represented by k_c in equation (3) determines the ease of lateral motion. Since the shear strength refers not only to the individual materials making up the interface but also to their interactions, it is often not possible to look it up from a reference. However, the limits of this value can easily be extracted as the second derivative of the DFT-based PES at its extrema.

(d) *Interfacial charge transfer:* the interaction at the interface has been shown to display a strong dependence on the charge accumulated at the interface as a result of the adhesion of the two surfaces [26]. In this context charge transfer refers to the depletion or excess of electrons that occurs in the space between the two components upon contact and is defined as

$$\Delta\rho(x, y, z) = \rho_{\text{tot}}(x, y, z) - \rho_{s1}(x, y, z) - \rho_{s2}(x, y, z) \tag{10}$$

where all three terms have similar interpretations to those in equation (9). Since the electronic density is a natural outcome of DFT calculations, this property can also easily be calculated with simple post-processing steps.

(e) *Load-dependent lateral forces and average friction coefficient:* the recipe commonly used in calculating load-dependent friction forces and the average friction is still the one outlined in the 1991 work by Zhong and Tománek [21]. The PES described above corresponds to zero load. Its generalization to finite load can be done by calculating the distance, say z', that corresponds to the desired load (F_L), which is simply the vertical component of the total force per area of the sliding surface. Since z' is expected to be different at each x and y, it has to be calculated at each point of travel during sliding. The friction force, by definition, is always along the direction opposite to the velocity of the sliding object. Therefore, the position-dependent friction force $F_f(x, y;\ F_L)$ for a given load can be calculated by summing the atomic force components in the direction opposite the direction of travel. The average friction force, F_f, will then be an average over the negative values of $F_f(x, y;\ F_L)$. In other words, positive lateral forces are excluded from the average. Finally, a friction coefficient analogous to the macroscopic definition can be calculated using the definition in equation (2).

Repeating this set of calculations for different loads, one then obtains the behavior of μ as a function of load.

(f) *Type of interaction:* the specific type of interaction between the components of an interface is material-dependent but is often a mixture of electrostatic and van der Waals (vdW) forces, with the exception of covalently-bonded pure bulk interfaces. Since the behavior of each type of interaction is different as a function of vertical separation (and by extension of the load) it is important to understand the extent to which each type of interaction contributes to the overall adhesion. Although vdW forces cannot be modeled directly with conventional DFT [37], several approximations have been developed [38–40] to describe them. In some of these approximations (see section 3), it is possible to separate the contribution of the vdW forces from the Coulombic interaction. This is a useful feature since it explains certain trends in lateral forces.

(g) *Defects, lubricants, support:* in a real interface, the components are never perfect. Unintentional or sometimes intentional defects affect the friction behavior for better or for worse. DFT-based methods have the ability to model defective materials just as easily as pristine ones. In particular, the charge and the charge density of the defect plays an important part in the interfacial interaction. Atomic charges can be assigned (albeit in an approximate manner) through postprocessing operations through methods such as Bader decomposition [41].

In a similar manner lubricants and their effect of friction and wear can be studied easily. A large portion of understanding lubricants lies in identifying their adsorption geometries. DFT forces, calculated utilizing the Hellman–Feynman theorem [42] can be followed, through standard geometry optimization algorithms, to the equilibrium geometry of the lubricants. Once the equilibrium is reached, in addition to analyzing bonding, partial charges etc, adsorption energies can also be calculated using

$$E_{\text{ads}} = E_{\text{tot}} - E_{\text{surf}} - E_{\text{mol}} \tag{11}$$

where E_{tot} is the total energy at the equilibrium configuration of the adsorbate, E_{surf} is the total energy of the isolated surface and E_{mol} is the total energy of the isolated molecule.

(h) *Tribochemistry:* the emerging field of *tribochemistry* deals with reactions that are facilitated by the pressure and relative motion of the materials making up the interface. Using tools such as nudged elastic bands [43] and *AIMD* [25], activation barriers can be calculated.

Thanks to the size of the domain of properties that can be calculated using DFT and the compromise it offers between accuracy and affordability, the literature on what can be referred to as *ab initio tribology* has grown rapidly over the past few decades [21, 26, 44, 45]. Before going into the body of literature on DFT-based treatment of nanotribological properties of materials, we give a brief introductory survey of DFT.

3. Basics of DFT and the treatment of weak interactions

In the last decades, DFT has emerged as the standard tool in computational chemistry and physics [46–48]. Earlier attempts to use the ground-state electron density, $n(\boldsymbol{r})$, to calculate the ground state electronic structure of atoms and molecules predates the fundamental theorems of Hohenberg and Kohn (HK) [22], which established DFT as an exact theory: see the Thomas–Fermi approximation of atomic physics [49], and the Xα scheme of Slater [50].

The modern version of DFT in use today is Kohn–Sham DFT [51] (KS-DFT), in which the exact ground state density of the system is constructed from a set of orbitals which are the eigenfunctions of a one-particle operator, the Kohn–Sham Hamiltonian. Within the Born–Oppenheimer approximation [52], and neglecting relativistic effects, the KS equations read:

$$\left(-\frac{1}{2}\nabla^2 + v_{\mathrm{KS}}(\boldsymbol{r})\right)\varphi_j(\boldsymbol{r}) = \varepsilon_j\varphi_j(\boldsymbol{r}), \tag{12}$$

where

$$v_{\mathrm{KS}}(\boldsymbol{r}) = v_{\mathrm{ext}}(\boldsymbol{r}) + \int \frac{n(\boldsymbol{r}')}{|\boldsymbol{r}-\boldsymbol{r}'|}\,\mathrm{d}\boldsymbol{r}' + v_{\mathrm{xc}}[n](\boldsymbol{r}). \tag{13}$$

In equation (13), $v_{\mathrm{ext}}(\boldsymbol{r})$ is the external potential, which comprises the electron–nuclear attractions, but can also include one-electron interactions terms (i.e. with external static electric fields). The second term is the Hartree potential, while $v_{\mathrm{xc}}[n](\boldsymbol{r})$ is the exchange–correlation potential, formally defined as the functional derivative of the exchange and correlation energy, E_{xc}:

$$v_{\mathrm{xc}}[n](\boldsymbol{r}) = \frac{\delta E_{\mathrm{xc}}}{\delta n(\boldsymbol{r})}. \tag{14}$$

The energy term E_{xc} derives from the following partition of the ground-state energy E:

$$E = T_{\mathrm{s}} + U + V_{\mathrm{ext}} + E_{\mathrm{xc}}[n], \tag{15}$$

where T_{S} is the kinetic energy of the non-interacting electrons, U is the Coulomb energy, and $E_{\mathrm{xc}}[n]$ contains everything else to make equation (15) exact. The HK theorems only assures that equation (15) can be written, but do not provide $E_{\mathrm{xc}}[n]$, which is, at present, unknown. If the latter were known, the exact ground-state density of the system of interacting electrons (and every observable that can be written as a functional of the density) could be calculated from a closed set of self-consistent equations, in a way much similar to the Hartree–Fock (HF) scheme, but with a lower computational cost.

Therefore, to make the KS scheme practical, $v_{\mathrm{KS}}(\boldsymbol{r})$ must be approximated, and failures of DFT are directly related to poor or inadequate approximations to the $v_{\mathrm{xc}}[n](\boldsymbol{r})$ term of equation (13).

The earliest approximation to $E_{\mathrm{xc}}[n]$, which was also introduced in the HK paper [22], goes under the name of local density approximation (LDA) [53, 54] which reads:

$$E_{\mathrm{xc}}[n] = \int \varepsilon_{\mathrm{xc}}^{\mathrm{hom}}(n(\boldsymbol{r}))n(\boldsymbol{r})\mathrm{d}\boldsymbol{r} \tag{16}$$

where $\varepsilon_{\mathrm{xc}}^{\mathrm{hom}} = \varepsilon_{\mathrm{x}}^{\mathrm{hom}} + \varepsilon_{\mathrm{c}}^{\mathrm{hom}}$ is the exchange (x) and correlation (c) energy per particle of the homogeneous electron gas, evaluated at the density $n(\boldsymbol{r})$ of the interacting electron system. Experience shows that LDA gives accurate equilibrium geometries but overestimates binding energies. The next approximation in Jacob's ladder is the generalised gradient approximation (GGA), which makes use also of the gradient of the density at any point. Earlier GGA functionals were PW86 [55] and PW91 [54], while the most common GGA potential used in materials science nowadays is PBE [56]. The most popular and accurate class of functionals in use nowadays include a fraction of exact exchange energy from HF theory, and for this reasons they are called hybrid functionals. By far the most popular choice of hybrid functional in the chemistry literature is the Becke, three-parameter Lee–Yang–Parr [57–59] which includes 20% of exact exchange, while the PBE0 functional [60, 61]

(which includes 25% of exact exchange) is a standard choice in materials science. Although more accurate, the use of this class of functionals is computationally mode demanding than standard LDA and GGA, due to the need to evaluate the exact exchange, especially when coupled with the use of plane waves or Slater basis sets. This prompted the introduction of a new class of functionals called meta-GGA [62], and which includes a contribution of the kinetic energy density of the KS orbitals. Recent developments include the introduction of random-phase approximation (RPA) [63] type of functionals, and the use of range-separated hybrids [64] within time-dependent DFT [65, 66], to describe charge-transfer electronic excitations.

The failure of DFT in describing weak vdW interactions within LDA and GGA functionals was well known since the nineties, due to the inadequate treatment of long-range behavior of electrons [67], and prevented application of the method to a large selection of materials (ranging from biomolecules to the physisorption of molecules on surfaces). Interfacial forces that, to a large extent, determine the tribological behavior of systems stems mostly from Coulombic or vdW interactions. Resulting from dynamical correlation effects between electrons, vdW forces cannot be described accurately by conventional exchange–correlation functionals used in DFT and even earlier density-based calculations. The efforts to remedy this shortcoming have been extensive and varied. The most commonly used methods today can be roughly classified into three groups: methods that extend the DFT functional with atom-pair potentials, methods that propose a new self-consistent exchange–correlation functional to include the vdW corrections, and methods that rely on partial diagrammatic summations within perturbation theory, specifically RPA [68]. While RPA-based approaches are more accurate, they are still too costly for routine use in large-scale problems. Therefore, we only concentrate on the former two methods mentioned.

vdW interaction refers to the electron correlation arising from the induced fluctuating dipole moments in the fragments of a full system. Also referred to as London forces, the asymptotic behavior of the interaction energy goes like R^{-6} with respect to the separation R between the fragments. Correction schemes which extend the DFT energy function by atomic pair potentials are based on an additive term that only depends on the positions of the nuclei. The correction term in these London-type, or DFT-D approaches has the general form [69]

$$E_{\mathrm{DFT-D}} = -\sum_{AB}\sum_{n=6,8,10,\ldots} s_n \frac{C_n^{AB}}{R_{AB}^n} f_{\mathrm{damp}}(R_{AB}) \tag{17}$$

where R_{AB} is the internuclear distance between the atom pair AB, C_n^{AB} is the average nth order dispersion coefficient and the scaling factors s_n are chosen to correct the short-range repulsive behavior particular to the exchange–correlation chosen. The damping function f_{damp} serves to attenuate the correction at short ranges. The DFT-D family of methods were initiated by the 2004 version, now referred to as DFT-D1 [70]. In this work, the energy correction included only the sixth order term with constant dispersion coefficients, C_6. In the next version published in 2006 [38], namely DFT-D2, C_6 coefficients used values derived from calculated polarizabilities. The DFT-D3 [71] version usually provides a much better accuracy than DFT-D2, since it incorporates explicitly the effects of molecular environment. Recently a new DFT-D4 variant has emerged [72] where the dispersion coefficients are calculated on-the-fly by means of a Mülliken decomposition of density to each atom. This is reminiscent of an earlier variant, DFT-TS, developed by Tkatchenko and Scheffler [73], where Hirshfield decomposition was utilized.

The other class of vdW-correction to DFT includes the reformulation of the exchange–correlation functional. A result of a long and illustrious history, detailed in the excellent review by Berland [74], this family of functionals aim to develop an approximation to the exact exchange and correlation functional while maintaining the correlations coming from dynamical fluctuations in the densities between fragments. While the most important feature of the vdW interactions is the asymptotic behavior, these functionals must also reproduce all other types of interactions present in the system. The most widely used variety of these functionals, the vdW-DF family [67, 75–77] separates the total exchange–correlation energy into two terms

$$E_{\mathrm{xc}}^{\mathrm{vdW-DF}}[n] = E_{\mathrm{xc}}^{0}[n] + E_{\mathrm{c}}^{\mathrm{nl}}[n] \tag{18}$$

where $E_{\mathrm{xc}}^{0}[n]$ represents the local exchange and correlation and $E_{\mathrm{c}}^{\mathrm{nl}}[n]$ covers the nonlocal correlations, which are responsible for the vdW interactions. While the local part is usually written as a sum of LDA and GGA variants of exchange and correlation, the nonlocal part is derived from the adiabatic connection [78]. Approximations are developed to the kernel in the adiabatic connection, which obey physical constraints such as time-reversal symmetry and cancellation of self energy [67]. The tuning of the local and the nonlocal parts have to be done simultaneously. Other than the earliest version of the vdW-DF family, namely vdW-DF0 [79], which was formulated to cover layered systems, successive improvements vdW-DF1 [67], vdW-DF2 [40] and the vdW-cx [76] variants have progressively developed better approximations to the nonlocal part as well as an improved treatment of the local part. Other well-known approaches to developing functionals to handle vdW interactions are BEEF-vdW [80] and the VV09 [81]/VV10 [82] variants of the vdW-DF family. A correct

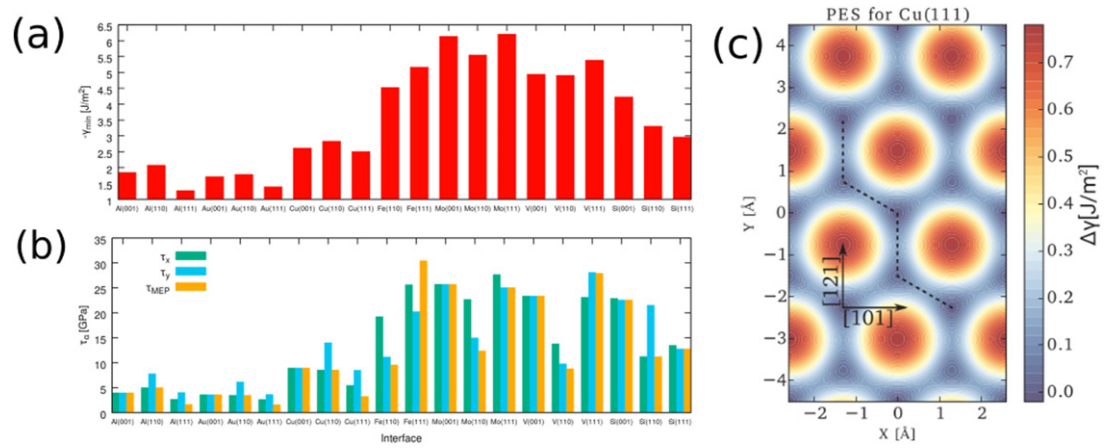

Figure 2. Reprinted from [85], Copyright (2018), with permission from Elsevier. Properties of a large number of interfaces calculated using DFT. (a) Separation energy, and (b) ideal shear strength of bulk interfaces. (c) The PES of the Cu(100)/Cu(100) interface.

description of vdW forces are at the center of most problems regarding atomic-scale tribology. As a result, possible variations with the vdW functionals chosen for a particular calculation must always be kept in mind.

4. Bulk interfaces

Defect-free interfaces formed by means of separating covalently-bonded bulk materials into two surfaces tend to present high adhesion energies and consequently, high friction forces. This is due to the perfect atomic coincidence and the tendency to form covalent bonds. As a result, use of bulk, non-layered materials in the context of tribology involve surface passivation or lubricants to reduce friction [83, 84]. Nevertheless, the DFT PES of bulk interfaces are important to act as a baseline in the efforts for reducing friction at these interfaces. A comprehensive study was conducted by Restuccia *et al* [85] where a large selection of perfect, symmetric bulk interfaces were investigated by means of a DFT-based workflow. The energy of separation was calculated by mapping the PES as seen in figure 2(c). In addition, the ideal shear strengths were obtained by numerical calculation of the second derivative of the energy with respect to distance for paths along x, y and the MEP. The results are displayed in the left panels of figures 2(a) and (b). The ideal shear strength and the energy of separation were found to correlate almost perfectly. Noble metals were seen to display lower separation energy while it was found to increase with increasing covalent character in the bonds. The Mo(111) surface was found to display the largest separation energy while the Au(111) surface was found to display the smallest.

A detailed study by Wolloch [26] investigated metallic, vdW bonded and covalently bonded crystal interfaces and established trends between the adhesion energy, interfacial charge and the corrugation. The results, summarized in figure 3, reveal that the interfacial charge redistribution upon adhesion, the adhesion energy and the corrugation all have strong positive correlation with one another. These results indicate that the adhesion, therefore corrugation, of vdW-bonded materials tend to be the lowest followed by metals, with the highest being covalently bonded materials. More accurately, the difference between displaced charge at the minimum and maximum of PES appears to determine the corrugation. Two outliers were identified, namely unreconstructed diamond (100) and (110) surfaces, whose corrugations are approximately a factor of 3 larger than the average covalently bonded material studied here. At the other end of the spectrum, the four vdW-bonded systems present corrugations that can be one order of magnitude lower than the next metallic system. In fact, two-dimensional materials are frequently utilized to reduce friction and wear due to their very low friction forces. We devote a separate section to this class of materials and their tribological properties later in our review (see section 5).

Due to the large friction forces at defect-free bulk interfaces, they are not suitable for applications that require moving parts sliding against one another. They are therefore often used together with surface-passivating species or lubricants. In the next two subsections, we review the DFT literature on these two modes of friction reduction.

4.1. Chemical passivation

Effects of the surface passivating species can be attributed to different phenomena including modification of the elastic properties, change in the PES, dissipation mechanisms due to difference in the mass of the passivating agents with respect to the host system atoms and charge redistribution [86]. Tran *et al* [45] explored the effect

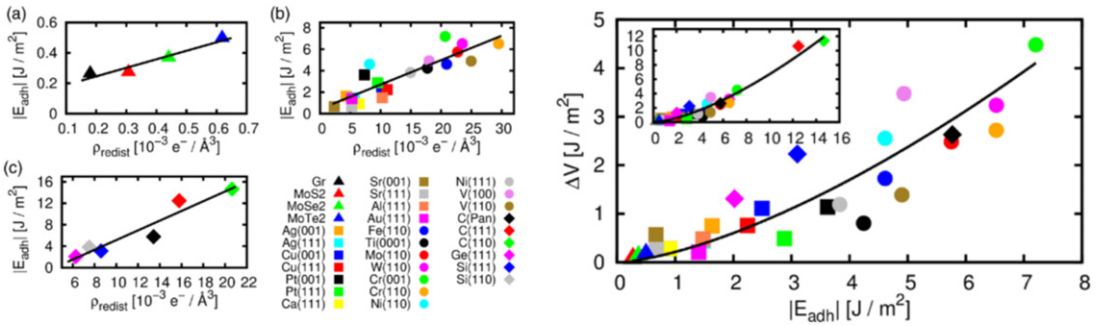

Figure 3. Reprinted (figure) with permission from [26], Copyright (2018) by the American Physical Society. Adhesion energy as a function of charge redistribution for (a) vdW-bonded materials, (b) simple and noble metals and (c) covalently bonded materials. The color representing each of the materials is given in the lower right. Rightmost panel: PES corrugation as a function of adhesion energy. The color coding is the same as that in the left panel.

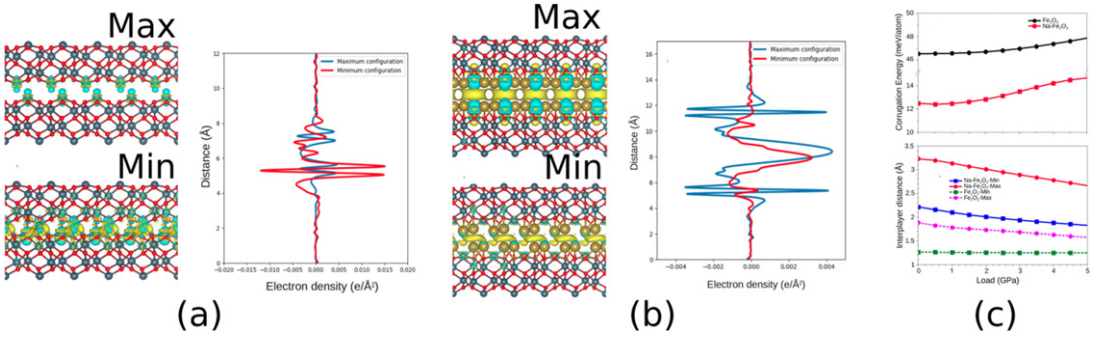

Figure 4. Reprinted from [45], with the permission of AIP Publishing. Three-dimensional and plane-averaged charge density difference for the least (Max) and most (Min) stable stacking configurations of the (a) clean, and (b) Na-passivated Fe_2O_3(0001) interface. The yellow and cyan represent the positive (electron accumulation) and negative (electron depletion) regions, respectively. (c) Corrugation energy and the interlayer distance for the same clean and passivated interfaces.

of Na atoms passivating a Fe_2O_3 interface. Figures 4(a) and (b) display the interface with and without the passivating Na agent, respectively. From these results, it is clear that the effect of the Na layer is two-fold. In addition to increasing the distance between the layers and thereby reducing the interaction, the Na layer also triggers a strong reorganization of the interfacial charge density. The positively charged Na atoms, as identified by Bader partial charge analysis, form a large barrier at both surfaces pushing an excess of electrons to the interfacial region (figure 4(b)). This results in a Coulombic repulsive interaction, which reduces the corrugation. In fact, the corrugation as a function of load as seen in figure 4(c) reduces dramatically in the presence of Na. Electronic structure methods are reliable in distinguishing the extent of electronic or steric effects as sources of friction reduction. A method for identifying the relative importance of these effects has been outlined by Reichenbach *et al* [86], where H and F terminated diamond and diamond-like surfaces were studied using an interatomic potential guided by DFT calculations. With the flexibility afforded by the ease of changing parameters in the interatomic potential, the effect of each parameter can be tested independently. As a result of this explorative work, steric effects were found to be the most important among all parameters.

The effects of passivation can also be enhanced by further doping. A striking example of this phenomenon was observed in the coefficient of friction of a phosphorous-doped H-terminated diamond film studied within the DFT-D2 framework [83]. Thanks to the H atoms, two opposing interfacial dipoles form at the interface of the C–H surfaces. This already causes a repulsion, decreasing the otherwise strong interaction between the diamond films. When the subsurface S dopant was introduced, it was seen to enhance the already existing dipole between the interfacial C and H atoms to such an extent that the coefficient of friction was found to diminish by at least an order of magnitude at low loads. In addition, the behavior of the doped and undoped interfaces as a function of load were shown to be completely the opposite: while the coefficient of friction was found to increase in the case of the doped interface with increasing load, it was shown to decreased in the undoped case.

Among other passivating scenarios studied are S- and P-terminated Fe surfaces [87], H-terminated diamond surfaces [88], and the F-terminated Cu/diamond interface [89]. The common theme shared by the

passivating agents, demonstrated clearly by electronic density difference and partial charge calculations, is the rearrangement of the charge density to increase the repulsion.

4.2. Lubricants

In addition to passivation, introducing lubricant species in the interface offers another effective way of reducing the friction as well as material loss due to wear. In general, lubricants are tailored to interact with both the lubricating liquid (placed at the interface to reduce wear) and the sliding surfaces. Depending on the particular needs of the setup, the lubricating films can be reactive or inert. A very large number of lubricants are available ranging from simple water [88] to complex organic [90] and inorganic polymers [91].

Understanding the properties of the lubricant requires insight into the adsorption of the lubricating species, the rearrangement of charge upon adsorption, any ensuing interdiffusion and/or tribochemical reactions between the lubricant and the surface, and the behavior of the lubricant under pressure and at high temperatures. While static DFT can be used reliably to understand the adsorption and structural properties of individual molecules of the lubricant, short *AIMD* runs conducted at high temperatures are usually sufficient to gain insight into the structural properties of the full lubricating film [91].

In the literature, DFT studies on lubricant films are conducted at many levels. While some studies reduce the problem to the most important features, others model the entire structure and experiment. For instance, Righi *et al* studied the effect of a simple film of P and S atoms on the Fe(110) surface to represent the behavior of the P and S atoms often found in many lubricants. They calculated the differences in shear and friction by means of calculating the PES of the P- and S-covered Fe(110) surface. At a slightly more complicated level, Blanck *et al* [92] calculated only the adsorption energies of possible lubricants on the γ–Al_2O_3 surface.

Inorganic glassy polymers used as lubricating films between Fe_2O_3 surfaces were studied extensively using DFT and AIMD [91]. In this study, the formation of the lubricating layer was studied from the ground up starting from a single P atom all the way to a full $NaPO_3$ layer. Bonding patterns, charge transfer and similar properties were identified, however, actual sliding simulations were not conducted. In a similar study, alkali metal borates at Fe_2O_3 interface [93] were investigated, however, this time static shear simulations were performed. During sliding, 'easy shear' structures were found to form, which refer to sliding-induced reorganization of the lubricating film in such a way that sliding is facilitated.

A similarly detailed and comparative DFT work was conducted on two common lubricating organic polymers, namely behenamide and cis-erucamide (figure 5(a)) [94]. Formally identical, the only difference between these two polymers is the double bond in cis-erucamide between C13 and C14. However, this difference causes cis-erucamide to exhibit much lower coefficients of friction. In reference [94], this difference was attributed to the difference in the stacking of polymers on the surface. Due to the π–π interaction between neighboring polymers, the polymer 'brush' formed on a graphene surface was found to be much denser. This prevents the molecules of the lubricating fluid to penetrate the polymer layer and lowers the friction.

A natural lubricant that is seen to reduce friction at the diamond interface is moisture, i.e. water [88]. In an AIMD calculation carried out on sliding surfaces with a water layer between them [95], Si centers doped into carbon and diamond-like films were found to accelerate hydroxylation and create a passivating surface (figure 5(b)). The simulations clearly associate the reduction of friction due to the water layer in between the sliding surfaces to the hydroxylation. In the absence of at least one surface with −OH termination, the water layer is stationary and contributes to friction. In contrast, surfaces hydroxylated with the help of Si dopants are seen to drag the water layer along and reduce friction in this way.

An alternative for friction reduction at the interface of sp^3-bonded carbon was suggested by the DFT study conducted by Wang *et al* [96]. A graphene layer inserted between two carbon surfaces was compared to the same surface but with hydrogen passivation instead. Graphene was seen to considerably lower the PES corrugation and display lower shear strength. The lower corrugation was attributed to the lower variation of charge transfer across the unit cell in the case of graphene.

Another commonly used class of lubricants is ionic liquids (ILs) [97]. An IL is a molten salt, consisting of large, polyatomic anion–cation pairs. When an IL is introduced as a lubricant in an interface, anions tend to form a layer in direct contact with the surface. Due to the electrostatic interaction, a cation layer follows. The interaction of the ILs with water is a second problem to consider since they can also react with water and hydrolize. In a joint experimental and DFT study conducted by Ba *et al* [98], four halogen-based ILs ([HMIM][Cl], [OMIM][Cl], [HMIM][Br], and [OMIM][Br]) were studied as lubricants between steel surfaces. Modeled using a Fe(100) surface in the DFT calculations, the adsorption characteristics of the ILs on the surface in the presence and absence of water were investigated. According to the DFT results, as seen in figure 5(c), [HMIM][Cl] binds to the surface through the N1–Fe bond. The second layer binds through electrostatic forces. At low water content, the N–Fe bonds remain strong, indicated by the bond lengths and adsorption energies. As the number of H_2O molecules increase, the bond length increases and the IL adsorption weakens. As a result, the efficacy of the lubricating IL layer decreases causing increased friction.

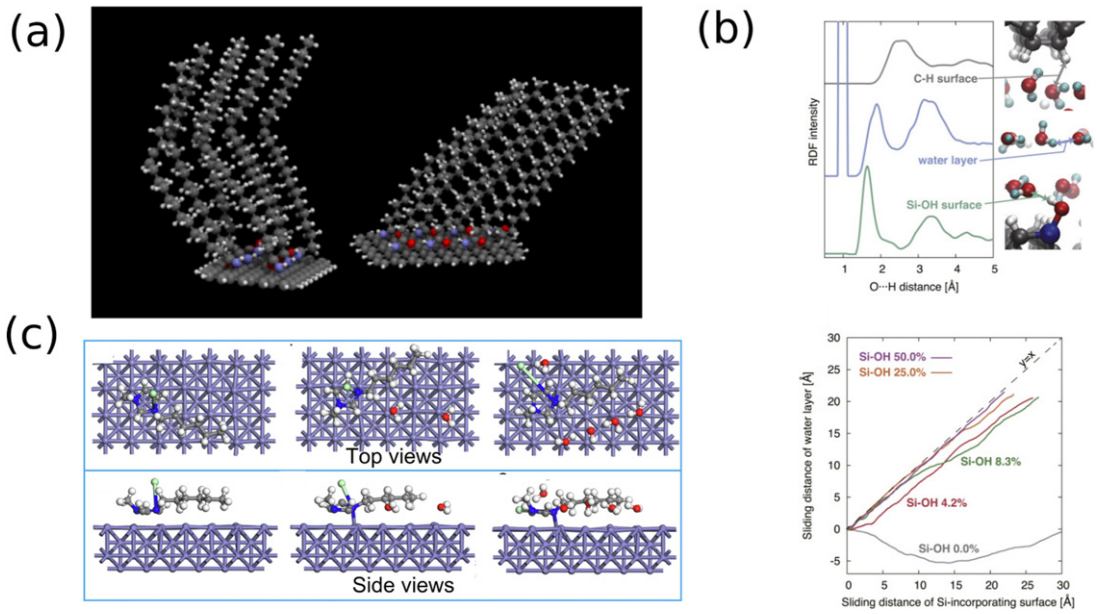

Figure 5. (a) Reprinted with permission from [94]. Copyright (2016) American Chemical Society. Geometry-optimized configurations of four erucamide (left) and behenamide (right) chains on a sheet of graphene. The 'brush' formed by erucamide is held together tighter due to the $\pi-\pi$ interaction. (b) Reprinted with permission from [95]. Copyright (2016) American Chemical Society. Top figure is a snapshot from an *AIMD* simulation of Si-doped C in water. The radial distribution of the O. . .H shown is on the left for both surfaces and the water layer inbetween. Bottom figure shows how far the water layer is dragged as a function of sliding distance of the Si-incorporating surface. (c) Reprinted with permission from [98]. Copyright (2020) American Chemical Society. Adsorption of the IL [HMIM][Cl] in the absence of water (left), [HMIM][Cl] + $2H_2O$ (center), and [HMIM][Cl] + $5H_2O$ (right) on the Fe(100) surface. Upper panels: top views; lower panels: side views.

Although friction at bulk interfaces and its reduction lies at the heart of many industrial endeavors, with the advances made in the fabrication and manipulation at the nanoscale, domains of tribology have extended to the lower dimensions. Since the successful modification of the AFM to handle also lateral forces, which we now refer to as the friction-force microscope (FFM) [4], friction at the nanoscale has exploded both in the experimental and the theoretical front. In the next section, we review the extensive literature on two-dimensional materials.

5. Two-dimensional materials

A class of materials that naturally exhibit low friction coefficient are two-dimensional, atomically thin films, which often derive from their layered bulk parent materials. Because of the remarkably low friction they display, two-dimensional films are often utilized as lubricants between bulk surfaces [99]. A good example to this property was presented by Cahangirov *et al* who showed, through DFT calculations, that graphene reduces sliding friction down to ultralow levels when inserted between bulk Ni(001) surfaces [44].

Chronologically speaking, the gateway to the immense diversity exhibited by the two-dimensional materials in the realm of nanotribology was certainly graphene. Tribological characteristics of single-layer, multi-layer, supported, pristine and defective graphene have been investigated in numerous experiments conducted by means of scan probe tools such as the FFM [100–106]. A range of friction coefficients ranging from 0.004 to 0.07 have been quoted, which, as a rule of thumb, indicate *ultralow friction*. In a particularly revealing experiment conducted by Feng *et al* [103], a graphene flake was found to travel in a straight line on a graphene layer between local PES minima formed by commensurate coincidence. This experiment was then reproduced by a MD study conducted by Sinclair *et al* [107], where low friction based on incommensurate coincidence was unquestionably demonstrated. Similar experimental work, albeit to a lesser extent was also conducted on MoS_2 [108, 109] and h-BN [110]. These experiments all indicate that due to the sensitive dependence of measurements on effects such as scanning tip size, substrate, degree of defectiveness and fabrication procedure, it is difficult to consistently pin down exact numbers for the lateral forces. In addition, even under the most ideal conditions, it is rather difficult to induce relative lateral motion between two sheets of material [30]. From this perspective, DFT calculations are of utmost utility in decoupling fundamental properties from external factors influencing the experimental outcome. Furthermore, DFT calculations can be used to narrow down the immense domain of available materials and identify candidate interfaces that could serve to minimize friction

in practical applications. For instance, the DFT work by Wang *et al* [111] identified the graphene/MoS_2 contact as an extremely low-friction surface due to the lack of charge density fluctuations during sliding.

The most fundamental property that can be easily understood by means of electronic structure methods is the PES. The corrugation of the PES defines an upper limit to kinetic friction in an ideal interface and therefore forms a baseline against which to compare experimental findings. In the following subsection, we discuss the PES of two-dimensional interfaces as identified by vdW-corrected DFT calculations.

5.1. The PES

Due to the challenges inherent in working with materials of a reduced dimensionality, experimental work is plagued with various unknowns. Simulations of these experiments, particularly with insight into electronic effects, is therefore crucial. In fact, most experimental studies nowadays include a supporting theoretical part [109, 110]. Luckily, the most important figure of merit, the PES, also turns out to be the most straightforward to obtain in the case of 2D materials. Unless a particularly large Moiré pattern is being investigated, PES calculations involve small periodic simulation cells and can therefore be generated and interpreted efficiently.

Due to their characteristic low PES corrugation and relatively high in-plane stiffness, the concept of superlubricity often arises in discussions of tribological properties of 2D materials. The term *superlubricity* technically refers to the case where the force to initiate sliding is very small, i.e., friction forces are very low. Whether the interface is superlubric depends both on the corrugation of the PES and the shear strength of the materials. However, in the literature, interfaces with an average static friction coefficient smaller than 0.01 have come to be referred to as exhibiting superlubric behavior [31]. Superlubricity can be achieved in two ways. *Structural superlubricity* occurs when the two materials forming the interface are incommensurate. In other words, there are no relative displacements at which the minima and the maxima of their PES coincide perfectly. Incommensurability in the interface can be due to a mismatch in the lattice constants of the materials or a relative rotation angle that disrupts perfect coincidence. On the other hand, *electronic superlubricity* is a result of inherently low corrugation caused by the electronic properties of the interface even in the presence of perfect structural commensurability. Both modes of superlubricity depend essentially on the flatness of the PES. In the study of two-dimensional systems, looking for superlubricity by means of determining the PES has thus become the standard approach [44].

As in the case of the bulk interface, the PES for interfaces composed of two-dimensional materials is often discussed in conjunction with interfacial charge redistribution [26]. The corrugation usually correlates with the difference in interfacial charges between the minima and maxima of the PES. In the case of the two-dimensional materials, the interaction can be broken down into different components, namely Coulomb and vdW forces, depending on the vdW correction employed.

The graphene/graphene PES has been calculated many times in the literature. One such comprehensive analysis was conducted by Reguzzoni *et al* [112]. The minimum, maximum and the saddle points are shown with the corresponding density difference maps in figure 6. As expected, the minimum and maximum of the PES correspond to AB (atom-on-hollow) and AA (atom-on-atom) stacking respectively, with a corrugation of approximately 10 meV/atom. This value, as shown by Reguzzoni *et al* and a similar work [113] depends sensitively on the vdW correction used (figure 6(a)). In both the AB and the AA stacking, charge is depleted from the interfacial gap (figures 6(b) and (c)) and accumulate on the sides of graphene layers that are facing one another. As the vertical load increases (or equivalently interlayer distance decreases), the two modes of stacking respond differently, namely while AA stacking does not exhibit large changes in the amount of depleted charge, AB displays increasing depletion. As a result, the corrugation increases with decreasing load.

In addition to interfacial electron density transfer, DFT calculations based on London-type vdW schemes also afford a way to understand the nature of the interaction. Wang *et al* [114] used DFT-D calculations to understand the relative contributions of the interfacial π–π and the vdW interactions. Since the vdW component in the DFT-D scheme is a position-dependent correction, it can easily be separated from the terms in the total energy. In this work, a H-terminated graphene square flake was positioned on a periodic graphene sheet and pulled along commensurate and incommensurate directions under a series of vertical loads. Both the top and bottom materials making up the interface were completely fixed eliminating any elastic contributions. As expected the corrugation along the incommensurate direction was about one-tenth of that along the commensurate direction. In addition, the repulsive π–π contribution to the energy was found to decrease while the vdW contribution increased with increasing load. Interestingly, along the incommensurate direction, the vdW contribution was not only much smaller than in the commensurate case but it varied much less.

Due to their identical atomic organization, h-BN is expected to display similar tribological properties to graphene. In a comparative work done by Gao *et al* [115], the adhesion energy, interlayer distance and corrugation at zero load were found to be very close. Their results are reproduced in figure 7. In contrast to the AB stacking in graphene, the minimum of the PES at zero load corresponds to the AA′ stacking where each

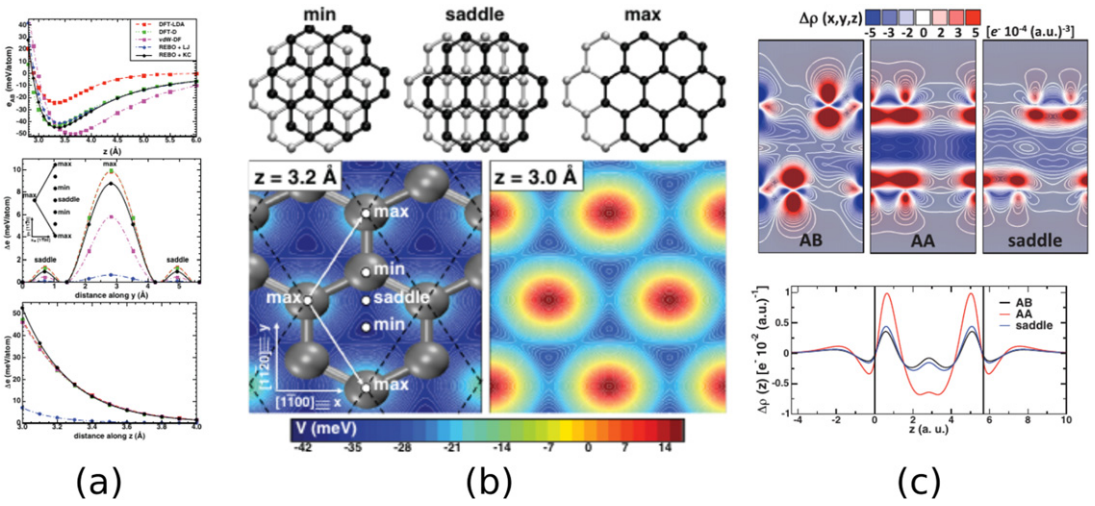

Figure 6. Reprinted (figure) with permission from [112], Copyright (2012) by the American Physical Society. Properties of the graphene–graphene interface. (a) Adhesion energy as a function of interlayer separation (top), PES along a straight path (middle) and zero-load separation along the same path (bottom). (b) The full two-dimensional PES at two different interlayer separations. (c) Charge density difference and its planar average corresponding to the extrema. Color codes are given in the figure.

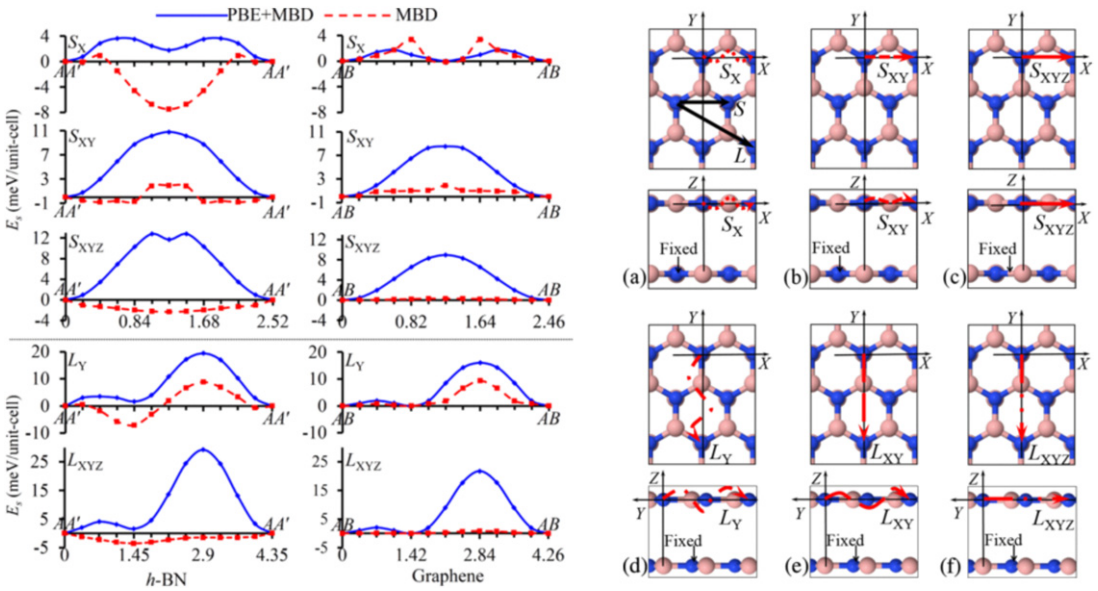

Figure 7. Reproduced from [115]. CC BY 3.0. Left panels: PES along the different sliding pathways shown in the right panels and described in the text for h-BN and graphene. Right panels: illustrations of the different paths followed for the PES mapping.

B in an h-BN layer is coincident with an N and vice versa. Starting from and ending at their respective preferred stacking configurations, graphene and h-BN layers were displaced along two paths (S and L in figure 7) and under three protocols (fixing the direction, fixing the x and y coordinates, and fixing x, y, and z coordinates) the corrugations were calculated. Albeit qualitatively similar, the h-BN sliding paths reveal slightly higher corrugations compared to graphene. A detailed analysis of the relative magnitudes of the Coulombic and vdW contribution to PES reveal interesting trends. The relative importance of the two contributions are highly protocol-dependent, where the zero-load MEP is almost entirely dictated by attractive vdW interactions for h-BN, while for graphene it is mostly repulsive and smaller. Along the constrained pathways, on the other hand, each contribution behaves similarly for h-BN and graphene, with the electrostatic forces being more important. While the single-atom-thick systems such as h-BN and graphene are widely used, a large majority of the two-dimensional systems have a more complex structure. Transition metal dichalcogenides (TMD, MX_2, M = metal, X = S, Se) have been shown to display about a third of the corrugation of graphene and h-BN interfaces [116, 117]. In contrast to strictly flat two-dimensional materials, dichalcogenides present a strong out-of-plane dipole moment, which increases the importance of Coulombic contributions to friction.

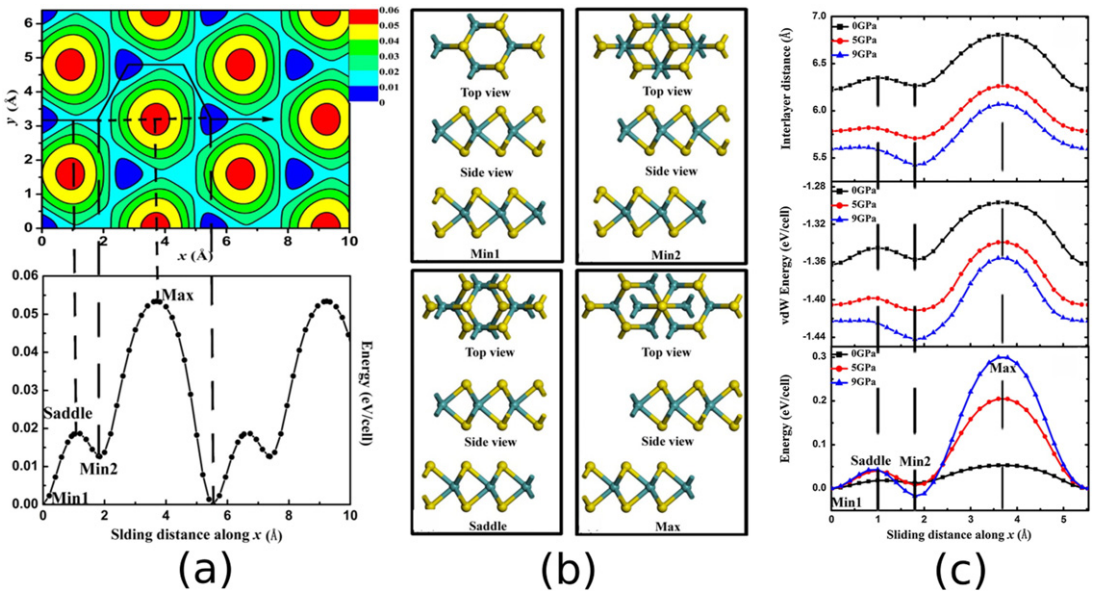

Figure 8. Reproduced from [119], with permission from Springer Nature. (a) The two-dimensional PES (top) and its one-dimensional cut along the sliding path indicated (bottom). (b) Configurations corresponding to the extrema marked on the PES. (c) The interlayer distance, the vdW energy, and the total energy along the same sliding path. Different lines correspond to different vertical loads as indicated in the figure.

For instance, the corrugation of the MoS_2 PES becomes more pronounced as the load increases thanks to Coulombic repulsion overcoming the vdW forces [118] (figure 8).

Although graphene, h-BN and TMDs are the most frequently studied materials, some less common two-dimensional materials have also displayed interesting features. Since most of these interfaces have yet to be synthesized, DFT PES calculations provide important insight and can be used as a guide for future experiments. Recently, ultralow friction was identified in puckered phosphorene films by Losi *et al* [120]. They tested two conventional (LDA and PBE) and three vdW-corrected (PBE + DF2 [40], PBE + D2 [38], and rVV10 [121]) exchange–correlation functionals in the calculation of some frictional figures of merit of phosphorene films. In this example, especially the charge redistribution and consequently the bilayer adhesion energy is seen to vary widely depending on the vdW correction scheme employed (figure 9). This, of course, is reflected in the other figures of merit such as the shear strength. Also, differences in the lattice constant calculated using the different schemes could play a role here.

In the work by Wang *et al* [122], Ca_2N, a novel two-dimensional material was investigated. In contrast to graphene, which is a zero gap metal [123], and h-BN and MoS_2, which have a finite band gap [124], the Ca_2N single layer is a full metal with two Ca bands crossing the Fermi level. When a bilayer is formed, an extra band appears at the Fermi level as a result of the interaction of the delocalized electron systems of the two layers at the interface. As a result, the band structure, in particular the dispersion of the interlayer bands turns out to be sensitive to vertical load. The mean force is smaller than a graphene–graphene interface for a large range of loads.

PES profiles mentioned in the works so far have all been calculated for perfect coincidence and therefore any superlubricity encountered is due to electronic effects. Friction along perfectly coincident pathways of symmetric (and therefore commensurate) interfaces are an upper limit to the friction experienced in an actual experiment. Structural superlubricity can be achieved through translating or rotating the two materials with respect to one another to obtain an incommensurate interface and the flattening of the PES. In fact DFT calculations on graphene [125] flakes display substantial decrease between coincident and noncoincident pathways.

Another way of creating low friction at two-dimensional interfaces is by means of constructing a hybrid interface between two different materials. However, periodic boundary conditions that are usually employed in simulations present an obstacle for the DFT investigations of these systems. Employing an affordable yet too small simulation cell may cause unrealistic strains for one or both of the materials. After all, strain has been proven to have a large effect on the tribological properties [118]. On the other hand, employing a simulation cell large enough to minimize the strain required to accommodate both materials could result in calculations that are too large to perform. Wang *et al* formulated a prediction of the necessary periodicity of the

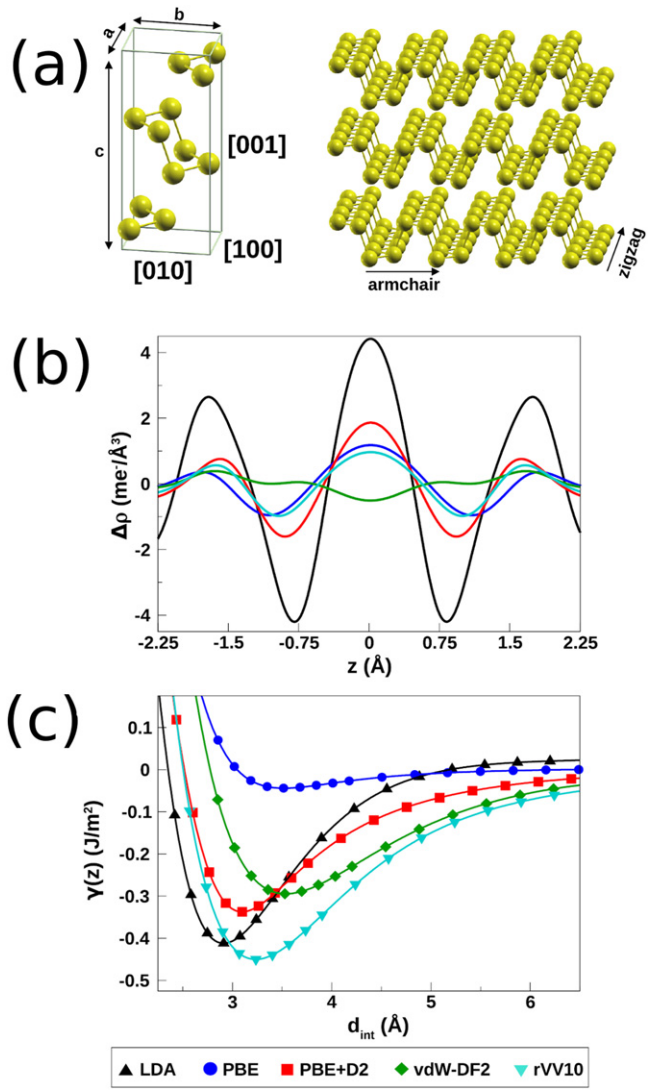

Figure 9. Reproduced from [120]. © IOP Publishing Ltd. CC BY 4.0. (a) Puckered phosphorene layers. (b) The corresponding charge redistribution. (c) Bilayer adhesion energy for different vdW correction schemes.

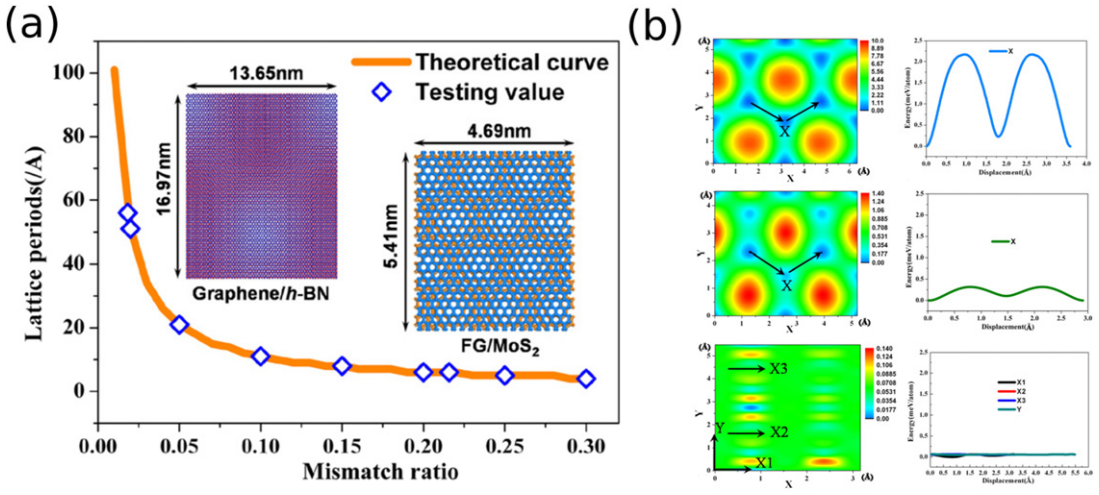

Figure 10. Reproduced from [31]. © IOP Publishing Ltd. All rights reserved. (a) The inverse relationship between the periodicity of the Moiré pattern and the lattice mismatch. (b) The PES of the FG/FG, MoS_2/MoS_2 and FG/MoS_2 interfaces.

Table 1. Corrugation values (meV/atom) calculated for interfaces in several computational studies are compared. P, HG and FG stand for phosphorene, fluorographene and hydrogenated graphene, respectively.

Interface type	Interface	ΔE	Source
Bulk	$Fe_2O_3(0001)/Fe_2O_3(0001)$	46.5	Reference [45]
Bulk/2D	Graphene/Cu(111)	≈12	Reference [126]
	h-BN/Au(111)	0.15	Reference [127]
2D	Graphene/graphene	≈10	Reference [112]
	h-BN/h-BN	≈10	Reference [115]
	MoS_2/MoS_2	≈3.3	Reference [119]
	HG/HG	0.96	Reference [128]
	FG/FG	0.31	Reference [128]
	P/P (AB stack.)	0.18 J m^{-2}	Reference [120]
	P/P (AZ stack.)	0.08 J m^{-2}	Reference [120]
	FG/MoS_2	0.14	Reference [31]
	$Graphene/MoS_2$	0.046	Reference [111]

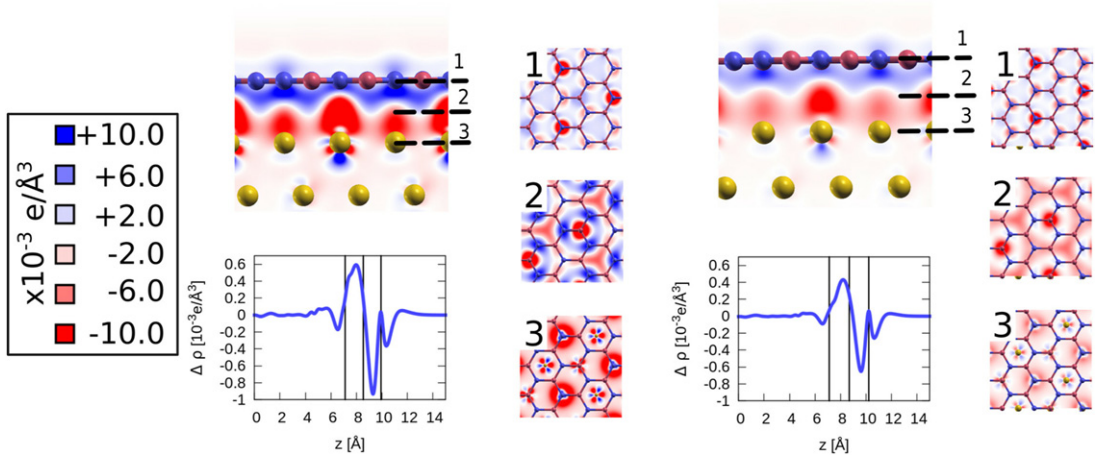

Figure 11. Reprinted with permission from [127]. Copyright (2019) American Chemical Society. The graphene–Au(111) interface. The charge density difference at a distance of $z = 2.8$ Å (left panels) and $z = 3.1$ Å (right panels) at the point $(x, y) = (0, 1.45)$ Å. Contour plots at three heights BN sheet (1), topmost Au layer (3) and the mid plane between the two materials (2) are also shown together with the plane-averaged charge density difference. On the plane-averaged $\Delta\rho$ plots the three planes are marked with vertical lines. Red areas represent an excess of negative charge and blue areas represent depletion.

Moiré pattern formed by the two materials as a function of the lattice mismatch [118]. The inverse relationship can be seen in figure 10(a). In spite of the large size, Wang *et al* present the DFT PES of the fluorinated graphene(FG)/MoS_2 interface, which has a corrugation much smaller than the corrugation of both the MoS_2 and the FG bilayers individually (figure 10(b)). Beside the materials mentioned here, the corrugation of a large number of interfaces have been calculated using DFT techniques. Table 1 lists DFT PES corrugation values of several interfaces involving 2D materials. For comparison, a few bulk interfaces have also been included.

Similarly to the bulk interfaces, several studies have linked the tribological behavior of interfaces to the interfacial charge density profile [26, 44, 129]. The majority of these studies focus on symmetric interfaces where both materials donate an equal amount of charge to the interface, whose magnitude determines the adhesion energy and friction forces. A highly symmetric interface, namely the h-BN/Au(111) interface, was modeled by Baksi *et al* [127] to simulate a sliding experiment between a gold-coated AFM tip and h-BN. This interface is between a metal and a material with polar bonds, and its charge profile at two different vertical separations ($d = 2.8$ Å and $d = 3.1$ Å) are also shown in figure 11. The interface appears to be highly polarized with an electron excess region near the Au(111) surface and an electron depletion region near the h-BN layer. Interestingly, the net electron charge is supplied by both materials. As a result, although the interface is polarized, its overall charge remains negative. It is also worth noting that although the amount of positive and negative charges are individually smaller for the $d = 3.1$ Å separation, the total integrated negative charge in the interface (defined as the distance between the top Au layer and the h-BN layer) increases from 1.0×10^{-5} e $Å^{-3}$ to 1.6×10^{-5} e $Å^{-3}$ going from $d = 2.8$ Å to $d = 3.1$ Å.

Before we conclude this subsection, we touch on the interesting behavior of the friction coefficients of two-dimensional interfaces under load. The load behavior of lateral friction forces as a function of load in 2D

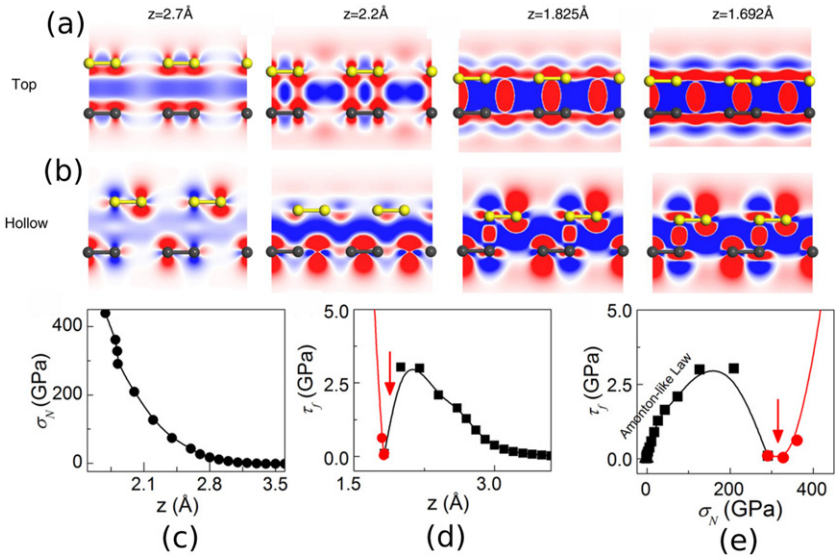

Figure 12. Reprinted with permission from [1]. Copyright (2018) American Chemical Society. (a) and (b) Pressure-dependent redistribution of electronic charge density (upper two panels). Red and blue represents electron accumulation and depletion, respectively, within a range of ± 0.01 e Å^{-3}. (a) Atom-on-atom stacking, and (b) middle atom-on-hollow stacking. The shift in the excess and depletion regions can be seen at $z = 1.825$ Å. The lowest panel displays the normal pressure (c), and shear pressure (τ_f) (d) as a function of distance as well as shear pressure as a function of normal pressure (e).

systems display a peculiar decreasing behavior with increasing load. This behavior, termed pressure-induced friction collapse by Sun *et al* [1] refers to the decrease and subsequent increase in the friction forces with increasing load. At high loads, interfacial interaction is governed by Coulombic forces. As the load increases, or in other words interlayer separation decreases, the interfacial charge variations reduce between minima and maxima and eventually charge depletion and excess regions switch. At the critical load where the switch happens, PES corrugations flatten and a very low friction force is observed, as seen in figure 12.

As seen in this section, a great deal of information can already be obtained about sliding interfaces by simple DFT PES calculations. However, there are other confounding factors that cause experiments to sometimes conflict. In the next section, we give examples of some of these factors and how they can be understood by using DFT calculations.

In spite of its importance, the PES alone is not sufficient to explain the observed tribological behavior of 2D materials. One important difference between measured and calculated friction forces (and even differences observed between different experimental setups) is the extra adhesion of the two-dimensional material around the edges of the tip beyond the apparent contact area as illustrated in figure 13. This puckering effect, often described as being similar to the bunching up of a carpet being swept by a vacuum cleaner, is larger for materials with high adhesion and low out-of-plane stiffness [24]. Therefore it is particularly pronounced in two-dimensional materials and is sensitive to the shape of the edge of the AFM tip. In a joint experimental and DFT investigation of the effect of the number of layers on friction forces in dichalcogenides [109], the intrinsic nanotribological behavior of one-, two- and three-layer films were successfully decoupled by estimating the puckering around the tip. In contrast to many studies, the tip was preworn to a flat edge rather than a sharp tip to eliminate the shape change during the experiment. The corrugation as a function of layer-thickness was calculated using DFT and the difference with experimental findings were successfully attributed to the effect of puckering. Figures 13(c)–(e) displays a clear dependence of friction on the thickness. In the DFT part of this work (figure 14), the PES profiles of the SiO_2 interface with dichalcogenides of one–three layers were calculated. The general trend of increasing friction with increasing layer number was recovered. The puckering effect can also be direction-dependent since along certain directions, formation of wrinkles may be easy. This was demonstrated in the graphene/graphene interface discussed by the joint experimental-DFT work by Almeida *et al* [130].

A natural way to disrupt the perfect graphene/graphene PES is the oxidation of each components. Although rather inert, it is possible to introduce certain oxygen-containing species to graphene's hexagonal network. The DFT calculations conducted by Wang *et al* [118] focus on graphene layers functionalized by epoxide and hydroxyl species. A very interesting set of results were reported where the corrugation was seen to increase in comparison to graphene. At the same time, shear strength was also seen to increase. In fact for a $C_8O(OH)$ flake sliding on a GO sheet, a corrugation increase of 20-fold and a shear strength increase of four-fold were

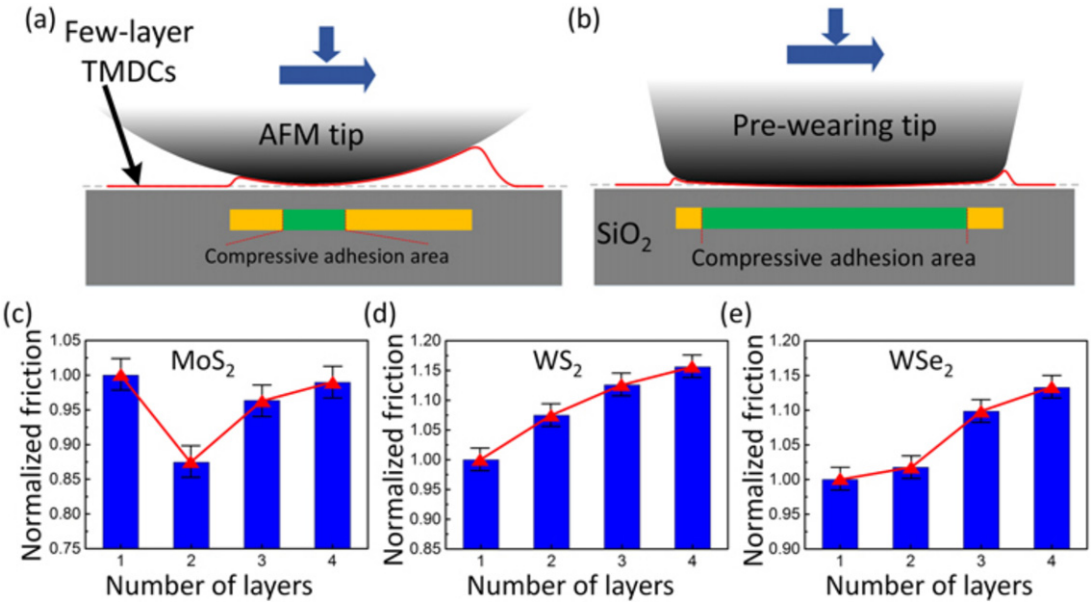

Figure 13. Reproduced from [109]. © IOP Publishing Ltd. All rights reserved. Schematic representation of the puckering effect for a sharp (a) and preworn tip (b). Normalized friction for the three materials as a function of layer number is shown in (c), (d) and (e).

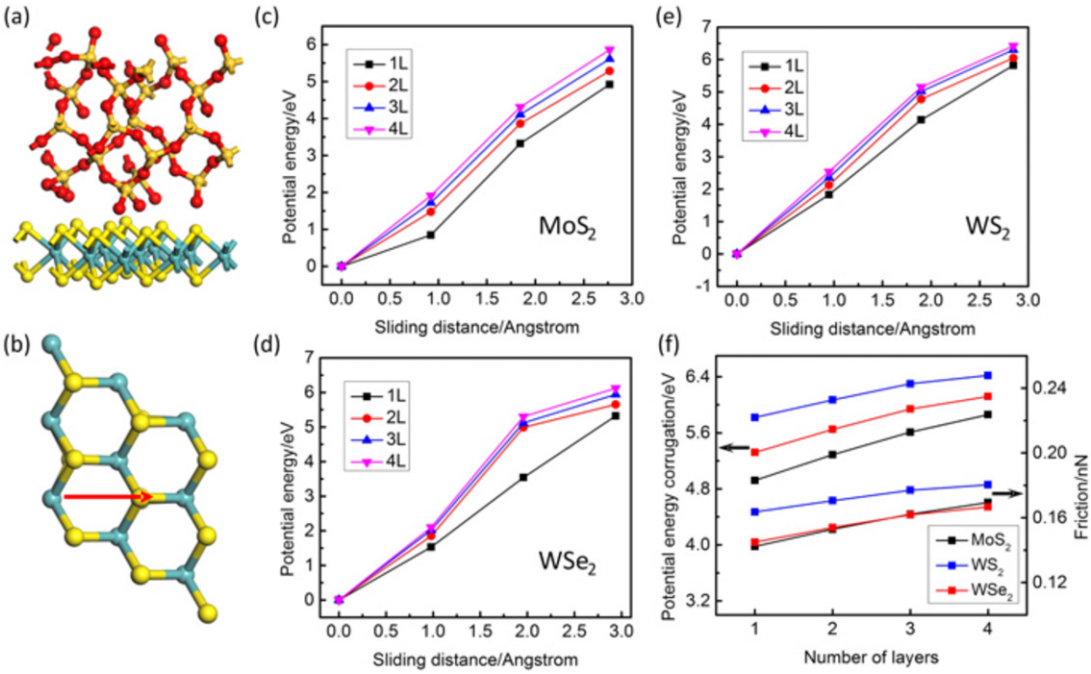

Figure 14. Reproduced from [109]. © IOP Publishing Ltd. All rights reserved. Atomistic models for the SiO_2/MoS_2 interface (a) and single MoS_2 layer(b). Friction force (normalized to the thinnest layer) due to the preworn tip is displayed for MoS_2 (c), WS_2 (d) and WSe_2 (e) as a number of layers. DFT studies (f) also confirm the experimental findings.

reported. The reason was attributed to the sp^2 to sp^3 change of hybridization upon functionalization with the foreign species and showed clearly in charge density difference calculations.

In the study of tribology, it is very difficult to model a realistic experimental setup with theoretical tools. The AFM geometries, the velocities and the ambient species are nearly impossible to simultaneously simulate in a realistic manner. This is even more difficult when it comes to electronic structure methods due to their accurate yet demanding nature. However, there are excellent examples of experimental work being supported by DFT calculations. In a study by Vazirisereshk *et al* [131], DFT was used to calculate the energy barrier of MoS_2/tip and graphene/tip interfaces to conclusively explain the differences in static friction observed in these two materials and their interfaces in AFM experiments. Similarly in the work by Falin *et al* [132], the differences

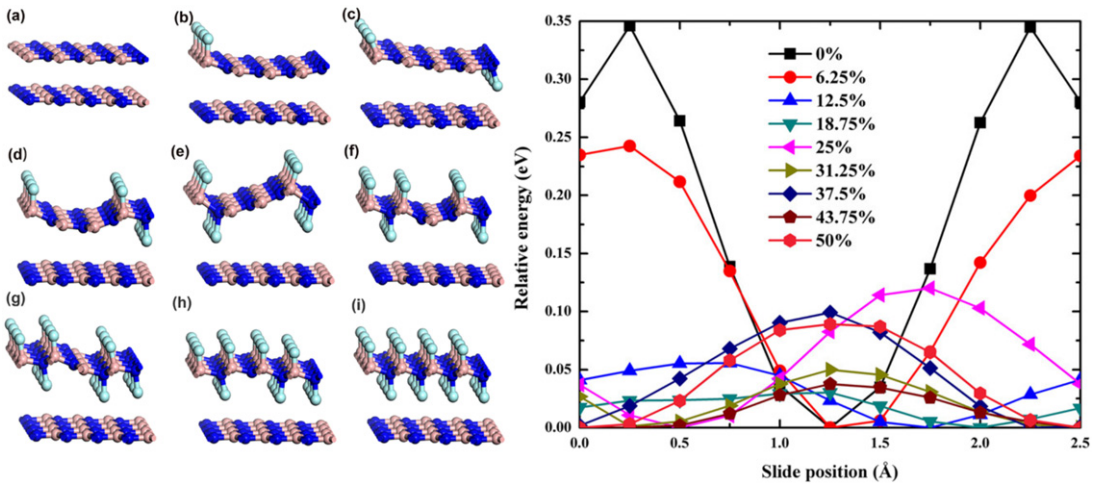

Figure 15. Reprinted from [24], with the permission of AIP Publishing. Geometries and corrugations of hBN sheets functionalized with F atoms at several ratios.

in sliding behavior between the graphene/graphene and the h-BN/h-BN interfaces were convincingly explained using both experimental work backed by DFT PES calculations.

5.2. Controlling friction at the nanoscale

The level of control offered by modern fabrication techniques results in the ability to manipulate interfaces to achieve even lower friction in commensurate interfaces. Ultralow friction can be achieved in two ways: structural and electronic. While the flattened PES of an incommensurate interface is a direct result of structural properties, a perfectly coincident symmetric interface can also present low friction due to its electronic structure.

As mentioned above, the electronic structure of bulk interfaces can be manipulated by means of chemical passivation. In general, species such as H or F are chosen in order to create or enhance surface dipoles. In a similar manner, the interfacial PES of two-dimensional materials can also be modified by means of covering the surface with suitable species. Investigation of F-Gr/MoS_2 [31], F-Gr/F-Gr [128, 133], H-Gr/H-Gr [128, 133], and O-Gr/O-Gr [128, 133] interfaces has revealed a consistent trend of reduced friction with respect to the graphene/graphene interface. In these studies, the surface species was mostly chosen to push the two materials away both sterically and electrostatically. In the F-enriched h-BN/h-BN interface investigated by Zhang *et al* [28], a different approach was taken where F was introduced at different ratios to disrupt the perfect PES and flatten it, figure 15. The particular geometry at each F ratio is determined by a DFT-driven geometry optimization and the PES was mapped (figure 15). The flattest PES was found for 18.75% F coverage, which yields the most asymmetric interface. 50% coverage was seen to bring the corrugation almost back to the level of the pristine h-BN/h-BN interface.

Cammarata *et al* argued that friction can also be modified at the chemical level by exchanging atoms strategically with lower- or higher-mass counterparts so as to lower the frequency of certain lattice vibration modes [116]. They utilized a property named *cophonocity* in the transition metal dichalcogenide family to extract atomic contributions to each phonon mode from a DFT calculation with vdW corrections. By means of exchanging those atoms that contribute the most to sliding-type phonon modes with lower mass counterparts, they suggested a way to tailor and control friction. The electronic structure at the interface can also be modified by external effects. It was shown that the PES of MoS_2/MoS_2 interface can be modified by electric field [119] and strain [118].

Tuning of the friction was achieved with a completely different method in the work by Pang *et al* [134], where graphene layers in graphite could be made to exhibit more or less friction by means of Li intercalation. In a similar manner, reduction of interfacial friction in commensurate graphene/h-BN heterostructures by surface functionalization was proven to work in the investigation by Guo *et al* [135]. To supplement the discussion of this section, and for an extensive review on the nanotribological properties of two-dimensional materials, we refer the reader to the review by Zhang *et al* [24].

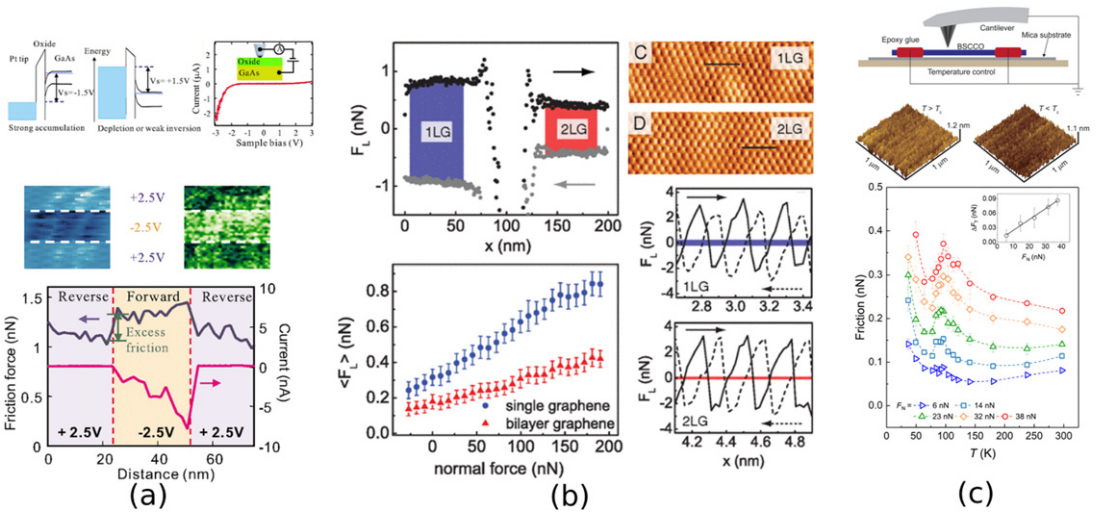

Figure 16. (a) Reprinted (figure) with permission from [136] Copyright (2008) by the American Physical Society. Schematic of the charge depletion/accumulation regions and the current-bias curve (top). Friction on a single layer graphene under reverse and forward bias as a function of sliding distance (bottom). (b) Reprinted (figure) with permission from [100], Copyright (2009) by the American Physical Society. Friction along the sliding path which covers both single-layer and bilayer graphene (top). Friction as a function of load along a linear path with continuously increasing load (bottom). (c) From [137]. © The Authors, some rights reserved; exclusive license AAAS. Distributed under a CC BY-NC 4.0. license Reprinted with permission from AAAS. The experimental setup (top) and friction as a function of temperature at various loads (bottom). The phase transition is clearly seen from the sudden change in the behavior.

6. Other topics

We conclude our overview on the applications of DFT-based methods in nanotribology by outlining a few topics that are of current research interest in the electronic structure community and that are likely to dominate future research efforts in the field. Of these, one already quite active is the identification of possible mechanisms of dissipation of the excess energy. In contact friction, caused by two sliding surfaces in relative motion with respect to one another, stick–slip events and asperities rubbing against one another create extra kinetic energy beyond what is thermally available. This excess energy will be dissipated via mechanisms in the substrates. The efficiency of this dissipation will determine the energy lost during motion.

The particular mechanism through which energy is dissipated remains a topic of debate, however, the most commonly accepted ones are phonons and electrons. In insulators, the phonon channels of energy dissipation are expected to be overwhelmingly prominent while in semiconductors and metals, electron–phonon interaction or electronic excitation events such as the formation of electron–hole pairs may be important [136]. Several experiments have been designed to identify conclusively the dominant channel of dissipation for a wide array of systems. Qi *et al* constructed a setup where an AFM tip made of Pt was made to slide across a GaAs surface backgated to a metal (figure 16(a)) in both the forward and reverse bias conditions. In the forward bias case, which corresponds to charge accumulation at the interface, excess friction was observed with respect to reverse bias. Eliminating various confounding factors such as change of effective load under bias, the excess friction was attributed to charged trapped states generated by the scanning tip.

Filleter *et al* [100] demonstrated the dissipation due to the electron–phonon interactions by means of measuring friction across a continuous junction made up of a single-layer and bilayer graphene. Scanning two materials as a part of the same setup eliminates setup-dependent unknowns such as change in the shape of the tip. The results indicate a marked decrease in friction in the bilayer sample with respect to the monolayer one due to a larger electron–phonon interaction, which acts to dampen the phonons and yield a more efficient dissipation mechanism (figure 16(b)).

In a recent experimental study, Wang *et al* [137] attempted to separate and identify the relative importance of electronic and phononic dissipation mechanisms using a Si nanotip sliding on the surface of a high-T_c bismuth strontium calcium copper oxide superconductor (figure 16(c)). The dissipation due to the Joule heating of electrons are expected to be eliminated below T_c. In fact, the friction coefficient above T_c and below T_c agree with the PT phononic dissipation model except for a continuous, positive offset for electronic friction for the normal state. In the immediate lower neighborhood of T_c a slow transition was observed as the number of normal-state electrons decrease. A combined temperature- and velocity-dependence for the friction forces was developed and formalized.

Since they are thought to be the main mechanism in many systems, phononic dissipation channels have been the subject of many more studies. De Mello *et al* [138] used the isotope effect, with deuterium substituting hydrogen, to isolate the phononic effects in amorphous carbon C/H thin films. In this work, the damping constant for phonon modes excited during sliding was modeled and estimated. Although Hu *et al* [139] argued that phononic dissipation can be due to the dephasing of harmonic phonons, most studies aim to uncover the anharmonic phonon–phonon interactions [140–144].

In the difficult task of identifying the underlying dissipation mechanisms, electronic structure methods can be valuable in determining phonon modes, frequencies, lifetimes and electron–phonon interaction parameters. The perturbative methods used in such calculations have been established decades ago and are now part of many mainstream software suites [145–147]. In a pioneering work by Sevinçli *et al* [144], the time evolution of the excess phonons generated was modeled in an interface between an infinitely large bulk material and a finite system. The model Hamiltonian was constructed in second quantization representation as:

$$\mathcal{H} = \sum_{j} \hbar\omega_j a_j^{\dagger} a_j + \sum_{\vec{k}} \hbar\omega_{\vec{k}} b_{\vec{k}}^{\dagger} b_{\vec{k}} + \sum_{\vec{k}j} \hbar(W_{\vec{k}j} b_{\vec{k}}^{\dagger} a_j + \text{h.c.}) \tag{19}$$

where $a_j^{\dagger}$ and $b_{\vec{k}}^{\dagger}$ are the creation operators associated with finite system vibration modes and infinite system phonons (in the single-branch approximation), respectively; $W_{\vec{k}j}$ is the coupling constant between the two systems and h.c. represents the Hermitian conjugate of the last term. Assuming either Lorentzian or geometric average coupling constants, the phonon populations were analyzed using three different methods, namely solving equations of motion of the phonon operators with the help of Laplace transforms, the Fano–Anderson method and the Green's function method. Some phonons modes were then artificially populated and their decay was monitored in time. Several practical examples were given, one of which concerns a model system with a single benzene molecule sliding along on a graphene sheet. DFT calculations were used to determined the equilibrium geometry of the benzene molecule as the vibration frequencies and eigenmodes. Assuming that the energy dissipation will mostly be carried out via the excitation of out-of-plane vibration modes, the coupling constants were also determined.

Several other environmental and experimental conditions affect the tribological behavior of interfaces in relative motion. Many of these effects have also been investigated using DFT calculations. Among these are the effects of the supporting substrate (especially in the case of two-dimensional materials) [148–150], defects [151–153], finite size effects such as the existence of edges [154], properties of the AFM tip [155,156] and the surrounding environment [157] including the effect of moisture. During the lifetime of a realistic system with sliding, the lubricant interacts with the surfaces and within itself. Sliding- and load-induced reactions can occur that changes the chemical makeup of the interface. Such reactions are the subject of an emerging field, namely tribochemistry. DFT and AIMD have already become staples of the modeling efforts in tribochemistry successfully modeling, for instance, TCP decomposition on Fe(110) [158] and the graphene/iron interface [159]. Exciting niche applications such as rolling friction [160, 161], spin friction [162] and friction modification via photoexcitation [163] are also explored.

Acknowledgments

The authors' work included in this review has received financial support from TÜBITAK, Scientific and Technological Research Council of Turkey (Grant No. 115F493).

Data availability statement

All data that support the findings of this study are included within the article (and any supplementary files).

References

[1] Sun J, Zhang Y, Lu Z, Li Q, Xue Q, Du S, Pu J and Wang L 2018 Superlubricity enabled by pressure-induced friction collapse *J. Phys. Chem. Lett.* **9** 2554–9

[2] Ptak F, Almeida C M and Prioli R 2019 Velocity-dependent friction enhances tribomechanical differences between monolayer and multilayer graphene *Sci. Rep.* **9** 14555
[3] Binnig G, Quate C F and Gerber C 1986 Atomic force microscope *Phys. Rev. Lett.* **56** 930–3
[4] Leggett G J, Brewer N J and Chong K S L 2005 Friction force microscopy: towards quantitative analysis of molecular organisation with nanometre spatial resolution *Phys. Chem. Chem. Phys.* **7** 1107–20
[5] Prandtl L 1928 Ein Gedankenmodell zur kinetischen Theorie der festen Körper *Z. Angew. Math. Mech.* **8** 85
[6] Tomlinson G A 1929 CVI.A molecular theory of friction *London, Edinburgh Dublin Phil. Mag. J. Sci.* **7** 905–39
[7] Popov V L and Gray J A T 2014 Prandtl–Tomlinson model: a simple model which made history *The History of Theoretical, Material and Computational Mechanics* (*Lecture Notes in Applied Mathematics and Mechanics* vol 1) (Berlin: Springer) pp 153–68
[8] Frenkel T and Kontorova Y 1939 On the theory of plastic deformation and twinning *Izv. Akad. Nauk, Ser. Fiz.* **1** 137–49
[9] Sokoloff J B 1990 Theory of energy dissipation in sliding crystal surfaces *Phys. Rev.* B **42** 760–5
[10] Sokoloff J B 1992 Theory of atomic level sliding friction between ideal crystal interfaces *J. Appl. Phys.* **72** 1262–70
[11] Sokoloff J B 1993 Theory of energy dissipation in sliding crystal surfaces at nonzero temperature *Phys. Rev.* B **47** 6106–9
[12] Vanossi A, Manini N, Urbakh M, Zapperi S and Tosatti E 2013 Colloquium: modeling friction: from nanoscale to mesoscale *Rev. Mod. Phys.* **85** 529–52
[13] Gigli L *et al* 2019 Detachment dynamics of graphene nanoribbons on gold *ACS Nano* **13** 689–97
[14] Xu L, Ma T-b, Hu Y-z and Wang H 2012 Molecular dynamics simulation of the interlayer sliding behavior in few-layer graphene *Carbon* **50** 1025–32
[15] Kim H, Venturini G and Strachan A 2012 Molecular dynamics study of dynamical contact between a nanoscale tip and substrate for atomic force microscopy experiments *J. Appl. Phys.* **112** 094325
[16] Varini N, Vanossi A, Guerra R, Mandelli D, Capozza R and Tosatti E 2014 Static friction scaling of physisorbed islands: the key is in the edge *Nanoscale* **7** 2093–101
[17] Wang J, Cao W, Song Y, Qu C, Zheng Q and Ma M 2019 Generalized scaling law of structural superlubricity *Nano Lett.* **19** 7735–41
[18] Khomenko A, Zakharov M and Persson B N J 2019 Frictional anisotropy of Al, Pt, and Pd nanoparticles on a graphene substrate *Tribol. Lett.* **67** 113
[19] Li L H, Chen Y, Behan G, Zhang H, Petravic M and Glushenkov A M 2011 Large-scale mechanical peeling of boron nitride nanosheets by low-energy ball milling *J. Mater. Chem.* **21** 11862–6
[20] Alhama F, Marín F and Moreno J A 2011 An efficient and reliable model to simulate microscopic mechanical friction in the Frenkel–Kontorova–Tomlinson model *Comput. Phys. Commun.* **182** 2314–25
[21] Tománek D, Zhong W and Thomas H 1991 Calculation of an atomically modulated friction force in atomic-force microscopy *Europhys. Lett.* **15** 887–92
[22] Hohenberg P and Kohn W 1964 Inhomogeneous electron gas *Phys. Rev.* **136** B864–71
[23] Vakis A I *et al* 2018 Modeling and simulation in tribology across scales: an overview *Tribol. Int.* **125** 169–99
[24] Zhang S, Ma T, Erdemir A and Li Q 2019 Tribology of two-dimensional materials: from mechanisms to modulating strategies *Mater. Today* **26** 67–86
[25] Iftimie R, Minary P and Tuckerman M E 2005 *Ab initio* molecular dynamics: concepts, recent developments, and future trends *Proc. Natl Acad. Sci. USA* **102** 6654–9
[26] Wolloch M, Levita G, Restuccia P and Righi M C 2018 Interfacial charge density and its connection to adhesion and frictional forces *Phys. Rev. Lett.* **121** 026804
[27] Berman D, Erdemir A and Sumant A V 2014 Graphene: a new emerging lubricant *Mater. Today* **17** 31–42
[28] Zhang J, Bai Y, An L, Zhang B, Zhang J, Yu Y and Wang C-M 2019 Reduction of interlayer friction between bilayer hexagonal boron nitride nanosheets induced by electron redistribution *J. Appl. Phys.* **126** 035104
[29] Manini N, Mistura G, Paolicelli G, Tosatti E and Vanossi A 2017 Current trends in the physics of nanoscale friction *Adv. Phys.* X **2** 569–90
[30] Baykara M Z, Vazirisereshk M R and Martini A 2018 Emerging superlubricity: a review of the state of the art and perspectives on future research *Appl. Phys. Rev.* **5** 041102
[31] Wang L-F, Ma T-B, Hu Y-Z, Zheng Q, Wang H and Luo J 2014 Superlubricity of two-dimensional fluorographene/MoS_2 heterostructure: a first-principles study *Nanotechnology* **25** 385701
[32] Fusco C and Fasolino A 2005 Velocity dependence of atomic-scale friction: a comparative study of the one- and two-dimensional Tomlinson model *Phys. Rev.* B **71** 045413
[33] Ye Z and Martini A 2014 Atomistic simulation of the load dependence of nanoscale friction on suspended and supported graphene *Langmuir* **30** 14707–11
[34] Schirmeisen A, Jansen L, Hölscher H and Fuchs H 2006 Temperature dependence of point contact friction on silicon *Appl. Phys. Lett.* **88** 123108
[35] Liu Z, Ma T and Liu L 2017 Optical-assistant characterization of friction anisotropy properties of single-crystal graphene domains *Tribol. Int.* **110** 131–9
[36] Cahangirov S, Ataca C, Topsakal M, Sahin H and Ciraci S 2012 Frictional figures of merit for single layered nanostructures *Phys. Rev. Lett.* **108** 126103
[37] Foster M E and Sohlberg K 2010 Empirically corrected DFT and semi-empirical methods for non-bonding interactions *Phys. Chem. Chem. Phys.* **12** 307–22
[38] Grimme S 2006 Semiempirical GGA-type density functional constructed with a long-range dispersion correction *J. Comput. Chem.* **27** 1787–99
[39] Sabatini R, Gorni T and de Gironcoli S 2013 Nonlocal van der Waals density functional made simple and efficient *Phys. Rev.* B **87** 041108
[40] Lee K, Murray E D, Kong L, Lundqvist B I and Langreth D C 2010 Higher-accuracy van der Waals density functional *Phys. Rev.* B **82** 081101
[41] Tang W, Sanville E and Henkelman G 2009 A grid-based Bader analysis algorithm without lattice bias *J. Phys.: Condens. Matter.* **21** 084204
[42] Feynman R P 1939 Forces in molecules *Phys. Rev.* **56** 340–3
[43] Henkelman G, Uberuaga B P and Jónsson H 2000 A climbing image nudged elastic band method for finding saddle points and minimum energy paths *J. Chem. Phys.* **113** 9901–4

[44] Cahangirov S, Ciraci S and Özçelik V O 2013 Superlubricity through graphene multilayers between Ni(111) surfaces *Phys. Rev.* B **87** 205428
[45] Tran N V, Tieu A K, Zhu H, Ta H T T, Le H M and Ta T D 2020 An *ab initio* study on the effects of Na passivation on friction reduction of an iron oxide surface *J. Appl. Phys.* **127** 065305
[46] Parr R G and Weitao Y 1989 *Density-Functional Theory of Atoms and Molecules* (Oxford: Oxford University Press)
[47] Gross E K U and Dreizler R M 1990 *Density Functional Theory: An Approach to the Quantum Many-Body Problem* (Berlin: Springer)
[48] Burke K 2012 Perspective on density functional theory *J. Chem. Phys.* **136** 150901
[49] March N H 1957 The Thomas–Fermi approximation in quantum mechanics *Adv. Phys.* **6** 1–101
[50] Slater J C 1951 A simplification of the Hartree–Fock method *Phys. Rev.* **81** 385–90
[51] Kohn W and Sham L J 1965 Self-consistent equations including exchange and correlation effects *Phys. Rev.* **140** A1133–8
[52] Born M and Oppenheimer R 1927 Zur Quantentheorie der Molekeln *Ann. Phys.* **389** 457–84
[53] Vosko S H, Wilk L and Nusair M 1980 Accurate spin-dependent electron liquid correlation energies for local spin density calculations: a critical analysis *Can. J. Phys.* **58** 1200–11
[54] Perdew J P and Wang Y 1992 Accurate and simple analytic representation of the electron–gas correlation energy *Phys. Rev.* B **45** 13244–9
[55] Perdew J P and Yue W 1986 Accurate and simple density functional for the electronic exchange energy: generalized gradient approximation *Phys. Rev.* B **33** 8800–2
[56] Perdew J P, Burke K and Ernzerhof M 1996 Generalized gradient approximation made simple *Phys. Rev. Lett.* **77** 3865–8
[57] Becke A D 1993 Density-functional thermochemistry: III. The role of exact exchange *J. Chem. Phys.* **98** 5648–52
[58] Lee C, Yang W and Parr R G 1988 Development of the Colle–Salvetti correlation-energy formula into a functional of the electron density *Phys. Rev.* B **37** 785–9
[59] Stephens P J, Devlin F J, Chabalowski C F and Frisch M J 1994 *Ab initio* calculation of vibrational absorption and circular dichroism spectra using density functional force fields *J. Phys. Chem.* **98** 11623–7
[60] Perdew J P, Ernzerhof M and Burke K 1996 Rationale for mixing exact exchange with density functional approximations *J. Chem. Phys.* **105** 9982–5
[61] Ernzerhof M and Scuseria G E 1999 Assessment of the Perdew–Burke–Ernzerhof exchange–correlation functional *J. Chem. Phys.* **110** 5029–36
[62] Sun J, Ruzsinszky A and Perdew J P 2015 Strongly constrained and appropriately normed semilocal density functional *Phys. Rev. Lett.* **115** 036402
[63] Eshuis H, Yarkony J and Furche F 2010 Fast computation of molecular random phase approximation correlation energies using resolution of the identity and imaginary frequency integration *J. Chem. Phys.* **132** 234114
[64] Toulouse J, Gerber I C, Jansen G, Savin A and Ángyán J G 2009 Adiabatic-connection fluctuation–dissipation density-functional theory based on range separation *Phys. Rev. Lett.* **102** 096404
[65] Runge E and Gross E K U 1984 Density-functional theory for time-dependent systems *Phys. Rev. Lett.* **52** 997–1000
[66] Burke K, Werschnik J and Gross E K U 2005 Time-dependent density functional theory: past, present, and future *J. Chem. Phys.* **123** 062206
[67] Dion M, Rydberg H, Schröder E, Langreth D C and Lundqvist B I 2004 Van der Waals density functional for general geometries *Phys. Rev. Lett.* **92** 246401
[68] Olsen T and Thygesen K S 2013 Random phase approximation applied to solids, molecules, and graphene–metal interfaces: from van der Waals to covalent bonding *Phys. Rev.* B **87** 075111
[69] Grimme S 2011 Density functional theory with London dispersion corrections *WIREs Comput. Mol. Sci.* **1** 211–28
[70] Grimme S 2004 Accurate description of van der Waals complexes by density functional theory including empirical corrections *J. Comput. Chem.* **25** 1463–73
[71] Grimme S, Antony J, Ehrlich S and Krieg H 2010 A consistent and accurate *ab initio* parametrization of density functional dispersion correction (DFT-D) for the 94 elements H-Pu *J. Chem. Phys.* **132** 154104
[72] Caldeweyher E, Bannwarth C and Grimme S 2017 Extension of the D3 dispersion coefficient model *J. Chem. Phys.* **147** 034112
[73] Tkatchenko A and Scheffler M 2009 Accurate molecular van der Waals interactions from ground-state electron density and free-atom reference data *Phys. Rev. Lett.* **102** 073005
[74] Berland K, Cooper V R, Lee K, Schröder E, Thonhauser T, Hyldgaard P and Lundqvist B I 2015 van der Waals forces in density functional theory: a review of the vdW-DF method *Rep. Prog. Phys.* **78** 066501
[75] Cooper V R 2010 Van der Waals density functional: an appropriate exchange functional *Phys. Rev.* B **81** 161104
[76] Berland K and Hyldgaard P 2014 Exchange functional that tests the robustness of the plasmon description of the van der Waals density functional *Phys. Rev.* B **89** 035412
[77] Klimeš J, Bowler D R and Michaelides A 2009 Chemical accuracy for the van der Waals density functional *J. Phys.: Condens. Matter.* **22** 022201
[78] Gunnarsson O and Lundqvist B I 1976 Exchange and correlation in atoms, molecules, and solids by the spin-density-functional formalism *Phys. Rev.* B **13** 4274–98
[79] Rydberg H, Lundqvist B I, Langreth D C and Dion M 2000 Tractable nonlocal correlation density functionals for flat surfaces and slabs *Phys. Rev.* B **62** 6997–7006
[80] Wellendorff J, Lundgaard K T, Møgelhøj A, Petzold V, Landis D D, Nørskov J K, Bligaard T and Jacobsen K W 2012 Density functionals for surface science: exchange–correlation model development with Bayesian error estimation *Phys. Rev.* B **85** 235149
[81] Vydrov O A and Van Voorhis T 2009 Nonlocal van der Waals density functional made simple *Phys. Rev. Lett.* **103** 063004
[82] Vydrov O A and Van Voorhis T 2010 Nonlocal van der Waals density functional: the simpler the better *J. Chem. Phys.* **133** 244103
[83] Wang J, Li M, Zhang X, Cai X, Yang L, Li J and Jia Y 2015 An atomic scale study of ultralow friction between phosphorus-doped nanocrystalline diamond films *Tribol. Int.* **86** 85–90
[84] Ta T D, Tieu A K, Zhu H, Zhu Q, Kosasih P B, Zhang J and Deng G 2016 Tribological behavior of aqueous copolymer lubricant in mixed lubrication regime *ACS Appl. Mater. Interfaces* **8** 5641–52
[85] Restuccia P, Levita G, Wolloch M, Losi G, Fatti G, Ferrario M and Righi M C 2018 Ideal adhesive and shear strengths of solid interfaces: a high throughput *ab initio* approach *Comput. Mater. Sci.* **154** 517–29
[86] Reichenbach T, Mayrhofer L, Kuwahara T, Moseler M and Moras G 2020 Steric effects control dry friction of H- and F-terminated carbon surfaces *ACS Appl. Mater. Interfaces* **12** 8805–16

[87] Righi M C, Loehlé S, De Barros Bouchet M I, Mambingo-Doumbe S and Martin J M 2016 A comparative study on the functionality of S- and P-based lubricant additives by combined first principles and experimental analysis *RSC Adv.* **6** 47753–60
[88] Zilibotti G and Righi M C 2011 *Ab initio* calculation of the adhesion and ideal shear strength of planar diamond interfaces with different atomic structure and hydrogen coverage *Langmuir* **27** 6862–7
[89] Liu Z, Zheng S, Lu Z, Pu J and Zhang G 2018 Adhesive transfer at copper/diamond interface and adhesion reduction mechanism with fluorine passivation: a first-principles study *Carbon* **127** 548–56
[90] Ta T D, Tieu A K and Tran B H 2021 Hydroxyl influence on adsorption and lubrication of an ultrathin aqueous triblock copolymer lubricant *Langmuir* **37** 1465–79
[91] Le M H, Tieu A K, Zhu H, Ta D T, Yu H, Ta T T H and Tran V N 2020 Surface transformation and interactions of iron oxide in glassy lubricant: an *ab initio* study *Chem. Phys.* **538** 110919
[92] Blanck S, Loehlé S, Steinmann S N and Michel C 2020 Adhesion of lubricant on aluminium through adsorption of additive head-groups on γ–alumina: a DFT study *Tribol. Int.* **145** 106140
[93] Ta H T T, Tieu A K, Zhu H, Yu H, Tran N V, Le H M and Ta T D 2020 Structural response of alkali metal borates at Fe_2O_3 sliding interface: the effect of alkali cations *Comput. Mater. Sci.* **184** 109930
[94] Hernández Velázquez J D, Barroso-Flores J and Gama Goicochea A 2016 *Ab initio* modeling of friction reducing agents shows quantum mechanical interactions can have macroscopic manifestation *J. Phys. Chem.* A **120** 9244–8
[95] Kajita S and Righi M C 2016 A fundamental mechanism for carbon-film lubricity identified by means of *ab initio* molecular dynamics *Carbon* **103** 193–9
[96] Wang J *et al* 2019 The flexible lubrication performance of graphene used in diamond interface as a solid lubricant: first-principles calculations *Nanomaterials* **9** 1784
[97] Cai M, Yu Q, Liu W and Zhou F 2020 Ionic liquid lubricants: when chemistry meets tribology *Chem. Soc. Rev.* **49** 7753–818
[98] Ba Z, Huang G, Qiao D and Feng D 2020 Experimental and calculation studies on the relationship between the hygroscopic behavior and lubrication properties of ionic liquids *Appl. Surf. Sci.* **529** 147031
[99] Xiao H and Liu S 2017 2D nanomaterials as lubricant additive: a review *Mater. Des.* **135** 319–32
[100] Filleter T, McChesney J, Bostwick a., Rotenberg E, Emtsev K, Seyller T, Horn K and Bennewitz R 2009 Friction and dissipation in epitaxial graphene films *Phys. Rev. Lett.* **102** 086102
[101] Filleter T and Bennewitz R 2010 Structural and frictional properties of graphene films on SiC(0001) studied by atomic force microscopy *Phys. Rev.* B **81** 155412
[102] Shin Y J, Stromberg R, Nay R, Huang H, Wee A T S, Yang H and Bhatia C S 2011 Frictional characteristics of exfoliated and epitaxial graphene *Carbon* **49** 4070–3
[103] Feng X *et al* 2013 Superlubric sliding of graphene nanoflakes on graphene *ACS Nano* **7** 1718–24
[104] Peng Y, Wang Z and Li C 2014 Study of nanotribological properties of multilayer graphene by calibrated atomic force microscopy *Nanotechnology* **25** 305701
[105] Marchetto D, Feser T and Dienwiebel M 2015 Microscale study of frictional properties of graphene in ultra high vacuum *Friction* **3** 161–9
[106] Paolicelli G, Tripathi M, Corradini V, Candini A and Valeri S 2015 Nanoscale frictional behavior of graphene on SiO_2 and Ni(111) substrates *Nanotechnology* **26** 055703
[107] Sinclair R C, Suter J L and Coveney P V 2018 Graphene–graphene interactions: friction, superlubricity, and exfoliation *Adv. Mater.* **30** 1705791
[108] Miura K and Kamiya S 2002 Observation of the Amontons–Coulomb law on the nanoscale: frictional forces between MoS_2 flakes and MoS_2 surfaces *Europhys. Lett.* **58** 610–5
[109] Fang L, Liu D-M, Guo Y, Liao Z-M, Luo J-B and Wen S-Z 2017 Thickness dependent friction on few-layer MoS_2, WS_2, and WSe_2 *Nanotechnology* **28** 245703
[110] Lee C, Li Q, Kalb W, Liu X-Z, Berger H, Carpick R W and Hone J 2010 Frictional characteristics of atomically thin sheets *Science* **328** 76–80
[111] Wang L *et al* 2017 Superlubricity of a graphene/MoS_2 heterostructure: a combined experimental and DFT study *Nanoscale* **9** 10846–53
[112] Reguzzoni M, Fasolino A, Molinari E and Righi M C 2012 Potential energy surface for graphene on graphene: *ab initio* derivation, analytical description, and microscopic interpretation *Phys. Rev.* B **86** 245434
[113] Kolmogorov A N and Crespi V H 2005 Registry-dependent interlayer potential for graphitic systems *Phys. Rev.* B **71** 235415
[114] Wang L, Ma T, Hu Y and Wang H 2016 Understanding the atomic-scale friction in graphene: the distinction in behaviors of interlayer interactions during sliding *J. Appl. Phys.* **120** 205302
[115] Gao W and Tkatchenko A 2015 Sliding mechanisms in multilayered hexagonal boron nitride and graphene: the effects of directionality, thickness, and sliding constraints *Phys. Rev. Lett.* **114** 096101
[116] Cammarata A and Polcar T 2015 Tailoring nanoscale friction in MX_2 transition metal dichalcogenides *Inorg. Chem.* **54** 5739–44
[117] Claerbout V E P, Polcar T and Nicolini P 2019 Superlubricity achieved for commensurate sliding: MoS_2 frictional anisotropy in silico *Comput. Mater. Sci.* **163** 17–23
[118] Wang C, Li H, Zhang Y, Sun Q and Jia Y 2014 Effect of strain on atomic-scale friction in layered MoS_2 *Tribol. Int.* **77** 211–7
[119] Wang C, Chen W, Zhang Y, Sun Q and Jia Y 2015 Effects of vdW interaction and electric field on friction in MoS_2 *Tribol. Lett.* **59** 7
[120] Losi G, Restuccia P and Righi M C 2020 Superlubricity in phosphorene identified by means of *ab initio* calculations *2D Mater.* **7** 025033
[121] Peng H, Yang Z-H, Perdew J P and Sun J 2016 Versatile van der Waals density functional based on a meta-generalized gradient approximation *Phys. Rev.* X **6** 041005
[122] Wang J, Li L, Shen Z, Guo P, Li M, Zhao B, Fang L and Yang L 2018 Ultralow interlayer friction of layered electride Ca_2N: a potential two-dimensional solid lubricant material *Materials* **11** 2462
[123] Kogan E, Nazarov V U, Silkin V M and Kaveh M 2014 Energy bands in graphene: comparison between the tight-binding model and *ab initio* calculations *Phys. Rev.* B **89** 165430
[124] Mak K F, Lee C, Hone J, Shan J and Heinz T F 2010 Atomically thin MoS_2: a new direct-gap semiconductor *Phys. Rev. Lett.* **105** 136805
[125] Bonelli F, Manini N, Cadelano E and Colombo L 2009 Atomistic simulations of the sliding friction of graphene flakes *Eur. Phys. J.* B **70** 449–59
[126] Toyoda K, Nozawa K, Matsukawa N and Yoshii S 2013 Density functional theoretical study of graphene on transition-metal surfaces: the role of metal d-band in the potential-energy surface *J. Phys. Chem.* C **117** 8156–60

[127] Baksi M, Toffoli D, Gulseren O and Ustunel H 2019 Nanotribological properties of the h-BN/Au(111) interface: a DFT study *J. Phys. Chem.* C **123** 28411–8
[128] Wang L-F, Ma T-B, Hu Y-Z, Wang H and Shao T-M 2013 *Ab initio* study of the friction mechanism of fluorographene and graphane *J. Phys. Chem.* C **117** 12520–5
[129] Wang J, Li J, Fang L, Sun Q and Jia Y 2014 Charge distribution view: large difference in friction performance between graphene and hydrogenated graphene systems *Tribol. Lett.* **55** 405–12
[130] Almeida C M *et al* 2016 Giant and tunable anisotropy of nanoscale friction in graphene *Sci. Rep.* **6** 31569
[131] Vazirisereshk M R *et al* 2019 Origin of nanoscale friction contrast between supported graphene, MoS_2, and a graphene/MoS_2 heterostructure *Nano Lett.* **19** 5496–505
[132] Falin A *et al* 2017 Mechanical properties of atomically thin boron nitride and the role of interlayer interactions *Nat. Commun.* **8** 15815
[133] Ko J-H, Kwon S, Byun I-S, Choi J S, Park B H, Kim Y-H and Park J Y 2013 Nanotribological properties of fluorinated, hydrogenated, and oxidized graphenes *Tribol. Lett.* **50** 137–44
[134] Pang Z, Wan J, Lu A, Dai J, Hu L and Li T 2020 Giant tunability of interlayer friction in graphite via ion intercalation *Extreme Mech. Lett.* **35** 100616
[135] Guo Y, Qiu J and Guo W 2016 Reduction of interfacial friction in commensurate graphene/h-BN heterostructures by surface functionalization *Nanoscale* **8** 575–80
[136] Qi Y, Park J Y, Hendriksen B L M, Ogletree D F and Salmeron M 2008 Electronic contribution to friction on GaAs: an atomic force microscope study *Phys. Rev.* B **77** 184105
[137] Wang W, Dietzel D and Schirmeisen A 2020 Single-asperity sliding friction across the superconducting phase transition *Sci. Adv.* **6** eaay0165
[138] De Mello S R S, Da Costa M E H M, Menezes C M, Boeira C D, Freire Jr F L, Alvarez F and Figueroa C A 2017 On the phonon dissipation contribution to nanoscale friction by direct contact *Sci. Rep.* **7** 3242
[139] Hu R, Krylov S Y and Frenken J W 2020 On the origin of frictional energy dissipation *Tribol. Lett.* **68** 8
[140] Buldum a, Leitner D M and Ciraci S 1999 Model for phononic energy dissipation in friction *Phys. Rev.* B **59** 16042–6
[141] Vink R L C 2019 Connection between sliding friction and phonon lifetimes: thermostat-induced thermolubricity effects in molecular dynamics simulations *Phys. Rev.* B **100** 094305
[142] Kwon O K, Kim H-W and Kang J W 2014 Energy exchange between vibration modes of a graphene nanoflake oscillator: molecular dynamics study *Curr. Appl. Phys.* **14** 237–44
[143] Wada N, Ishikawa M, Shiga T, Shiomi J, Suzuki M and Miura K 2018 Superlubrication by phonon confinement *Phys. Rev.* B **97** 161403
[144] Sevinçli H, Mukhopadhyay S, Senger R T and Ciraci S 2007 Dynamics of phononic dissipation at the atomic scale: dependence on internal degrees of freedom *Phys. Rev.* B **76** 205430
[145] Baroni S, de Gironcoli S, Dal Corso A and Giannozzi P 2001 Phonons and related crystal properties from density-functional perturbation theory *Rev. Mod. Phys.* **73** 515–62
[146] Gibbons T M, Bebek M B, Kang B, Stanley C M and Estreicher S K 2015 Phonon–phonon interactions: first principles theory *J. Appl. Phys.* **118** 085103
[147] Giustino F 2017 Electron–phonon interactions from first principles *Rev. Mod. Phys.* **89** 015003
[148] Shi R *et al* 2017 Moiré superlattice-level stick–slip instability originated from geometrically corrugated graphene on a strongly interacting substrate *2D Mater.* **4** 025079
[149] Christian M S and Johnson E R 2018 Effect of a metal substrate on interlayer interactions in bilayer graphene *J. Phys. Chem.* C **122** 8910–8
[150] Ta H T T, Tieu A K, Zhu H, Yu H and Tran N V 2021 A first-principles study of impurity-enhanced adhesion and lubricity of graphene on iron oxide surface *J. Phys. Chem.* C **125** 4310–21
[151] Zhang B, Zhang G, Cheng Z, Ma F and Lu Z 2019 Atomic-scale friction adjustment enabled by doping-induced modification in graphene nanosheet *Appl. Surf. Sci.* **483** 742–9
[152] Cheng Z, Zhang G, Zhang B, Ma F and Lu Z 2018 Tuning the electronic structure of hexagonal boron nitride by carbon atom modification: a feasible strategy to reduce sliding friction *Mater. Res. Express* **6** 036306
[153] Yang Z, Bhowmick S, Sen F G, Banerji A and Alpas A T 2018 Roles of sliding-induced defects and dissociated water molecules on low friction of graphene *Sci. Rep.* **8** 121
[154] Brndiar J, Turanský R, Dietzel D, Schirmeisen A and Štich I 2011 Understanding frictional duality and bi-duality: Sb-nanoparticles on HOPG *Nanotechnology* **22** 085704
[155] Gao L, Ma Y, Liu Y, Song A, Ma T, Hu Y, Su Y and Qiao L 2017 Anomalous frictional behaviors of Ir and Au tips sliding on graphene/Ni(111) substrate: density functional theory calculations *J. Phys. Chem.* C **121** 21397–404
[156] Chen J and Gao W 2017 Unconventional behavior of friction at the nanoscale beyond Amontons' law *ChemPhysChem* **18** 2033–9
[157] Arif T, Yadav S, Colas G, Singh C V and Filleter T 2019 Understanding the independent and interdependent role of water and oxidation on the tribology of ultrathin molybdenum disulfide (MoS_2) *Adv. Mater. Interfaces* **6** 1901246
[158] Osei-Agyemang E, Berkebile S and Martini A 2018 Decomposition mechanisms of anti-wear lubricant additive tricresyl phosphate on iron surfaces using DFT and atomistic thermodynamic studies *Tribol. Lett.* **66** 48
[159] Restuccia P and Righi M C 2016 Tribochemistry of graphene on iron and its possible role in lubrication of steel *Carbon* **106** 118–24
[160] Zhang B, Cheng Z, Lu Z, Zhang G and Ma F 2020 Atomic-scale rolling friction and charge-transfer mechanism: an integrated study of physical deductions and DFT simulations *J. Phys. Chem.* C **124** 8431–8
[161] Chen Y, Guo C-S, Gao W and Jiang Q 2020 Effective scheme for understanding rolling and sliding at nanoscale *Carbon* **161** 269–76
[162] Cai X, Wang J, Li J, Sun Q and Jia Y 2016 Spin friction between Co monolayer and Mn/W(110) surface: *ab initio* investigations *Tribol. Int.* **95** 419–25
[163] Liu X, Li Y and Guo W 2020 Friction modulation via photoexcitation in two-dimensional materials *ACS Appl. Mater. Interfaces* **12** 2910–5